Positivity-preserving Lagrangian scheme for multi-material compressible flow

Juan Cheng[1] and Chi-Wang Shu[2]

Abstract

Robustness of numerical methods has attracted an increasing interest in the community of computational fluid dynamics. One mathematical aspect of robustness for numerical methods is the positivity-preserving property. At high Mach numbers or for flows near vacuum, solving the conservative Euler equations may generate negative density or internal energy numerically, which may lead to nonlinear instability and crash of the code. This difficulty is particularly profound for high order methods, for multi-material flows and for problems with moving meshes, such as the Lagrangian methods. In this paper, we construct both first order and uniformly high order accurate conservative Lagrangian schemes which preserve positivity of physically positive variables such as density and internal energy in the simulation of compressible multi-material flows with general equations of state (EOS). We first develop a positivity-preserving approximate Riemann solver for the Lagrangian scheme solving compressible Euler equations with both ideal and non ideal EOS. Then we design a class of high order positivity-preserving and conservative Lagrangian schemes by using the essentially non-oscillatory (ENO) reconstruction, the strong stability preserving (SSP) high order time discretizations and the positivity-preserving scaling limiter which can be proven to maintain conservation and uniformly high order accuracy and is easy to implement. One-dimensional and two-dimensional numerical tests for the positivity-preserving Lagrangian schemes are provided to demonstrate the effectiveness of these methods.

AMS subject classification: 65M08, 76N15

Keywords: Lagrangian method; multi-material compressible flow; positivity-preserving; high order accuracy; general equation of state

[1]Laboratory of Computational Physics, Institute of Applied Physics and Computational Mathematics, Beijing 100088, China. E-mail: cheng_juan@iapcm.ac.cn. Research is supported in part by NSFC grants 10931004, 91130002 and 10972043. Additional support is provided by the National Basic Research Program of China under grant 2011CB309702 and CAEP under the project 2012A0202010.

[2]Division of Applied Mathematics, Brown University, Providence, RI 02912. E-mail: shu@dam.brown.edu. Research is supported in part by AFOSR grant F49550-12-1-0399 and NSF grant DMS-1112700.

1 Introduction

There are two typical frameworks to describe the motion of fluid flow, that is, the Eulerian framework and the Lagrangian framework. In the Eulerian formulation the mesh is fixed in space, which makes these methods very suitable for flows with large deformations. In fact, numerical methods for the equations of compressible fluid flow in Eulerian coordinates have been extensively investigated and they have the widest fields of applications. On the other hand, Lagrangian methods, e.g. [3, 4, 5, 19, 20], in which the computational mesh moves with the fluid, are more suitable for problems involving interfaces between materials or free surfaces. Thus they are widely used in many fields for multi-material flow simulations. Unfortunately, multidimensional extensions of Lagrangian methods are more difficult than those in the Eulerian case. To simulate flows with deformation, the Lagrangian methods are often combined with an algorithm to rezone the mesh and remap variables from the Lagrangian mesh to the rezoned mesh to avoid severe mesh distortion or mesh tangling which may destroy the calculations. This combined method that can choose the motion of the grid more freely is called the Arbitrary Lagrangian-Eulerian (ALE) method.

As computational fluid dynamics is widely used in many scientific and engineering fields, issues such as reliability and robustness of computations become more important. One mathematical aspect of scheme robustness is the positivity-preserving property. As in a conservative approximation to Euler equations where density, momentum and total energy are solved directly, the kinetic energy is computed from mass and momentum and then subtracted from the total energy. At high Mach numbers, internal energy appears as the small difference of two large quantities, and is therefore prone to large percentage errors. It may easily become negative numerically which may lead to nonlinear instability and a failure of the numerical scheme. An alternative way to solve this problem is the usage of a non-conservative scheme which solves the internal energy instead of the total energy directly, but its cost is the possible loss of conservation which may result in a wrong shock position or an exponential error growth.

A scheme is called positivity-preserving if it can update new states with positive density, internal energy and other physically positive variables, when starting from a set of physically admissible states. Numerous studies exist in the literature on this issue, especially for the Eulerian methods. In the earlier years, many first order positivity-preserving Eulerian schemes were well documented, for example, the classical Godunov scheme [9], Lax-Friedrichs scheme [23, 29], the modified HLLE scheme [9], the HLLC scheme [1], the AUSM+ scheme [17], and the flux vector splitting schemes such as Van Leer's and Steger and Warming's [13]. Many gas-kinetic schemes have also been shown to be positivity-preserving, such as those in [21, 27]. Some of them are designed up to second order accuracy, e.g., [16, 22, 23, 10]. More recently, Zhang and Shu developed a series of high order positivity-preserving Eulerian schemes such as the Runge-Kutta discontinuous Galerkin (RKDG) method, weighted essentially non-oscillatory (WENO) finite volume and finite difference schemes [29, 30, 31, 32]. The part of our work in this paper on high order schemes is an extension of the work of Zhang and Shu to Lagrangian methods and to multi-material flows.

Numerical simulation of compressible multi-material flows arises in many applications including astrophysics, inertial confine fusion, underwater bubble dynamics, shock wave interactions with material interface and combustion, and so on. In these problems, large density jumps or strong pressure jumps across the material interface frequently happen which makes positivity-preserving a big issue for the simulation of this kind of multi-material fluid flows. Moreover, multi-material fluid flow may involve different kinds of equations of state (EOS), some of which are quite more complicated than the ideal EOS which is applied for perfect gas, for example, the stiffened EOS for water and the Jones-Wilkins-Lee (JWL) EOS for the detonation-products gas, which makes positivity-preserving more difficult to achieve. For this reason, positivity-preserving Eulerian schemes have seldom been discussed for multi-material problems.

Compared with Eulerian methods, positivity-preserving Lagrangian schemes are less investigated. The pioneering work on this issue includes the positivity-preserving Godunov-

type Lagrangian scheme based on the modified HLL Riemann solver [20], and the positive and entropic schemes for a general class of Lagrangian systems including gas dynamics and magnetohydrodynamics (MHD) in [2, 12]. Unfortunately all of these schemes are only first order accurate and only valid in one-dimensional space. As all of them adopt the mass coordinate, which can be implemented only in one-dimensional space. It is not clear how these schemes can be extended to higher dimensional spaces. The main difficulty is that Lagrangian fluxes should not introduce any numerical diffusion for density (no mass transfer between cells), hence many popular Eulerian fluxes such as Lax-Friedrichs fluxes are ruled out. It is significantly more difficult to prove the positivity-preserving property if the numerical flux does not have any diffusion for the first component (density).

In this paper, we will discuss the methodology to construct positivity-preserving Lagrangian schemes both in one- and in two-dimensional spaces, which can be used to simulate multi-material problems both with ideal EOS and non-ideal EOS. To be more specific, we first develop a HLLC approximate Riemann solver for the Lagrangian scheme which can preserve the positivity of density and internal energy (or a similar quantity which should be physically positive for some complicated EOS) in the simulation of multi-material flows with general equations of state. This HLLC numerical flux has a particularly simple form in the Lagrangian form. Based on this HLLC numerical flux, a class of first order positivity-preserving Lagrangian schemes is designed. We then design a class of high order positivity-preserving Lagrangian schemes by using the essentially non-oscillatory (ENO) reconstruction, the strong stability preserving (SSP) high order time discretizations and the positivity-preserving scaling limiter which can be proven to maintain conservation and uniformly high order accuracy both in one and two dimensions. One- and two-dimensional numerical tests for the positivity-preserving Lagrangian schemes are provided to demonstrate the effectiveness of these methods.

An outline of the rest of this paper is as follows. In Section 2, we describe the positivity-preserving HLLC approximate Riemann solver for the Lagrangian method solving compress-

ible Euler equations with general EOS and present a class of first order positivity-preserving Lagrangian schemes both in one and two spatial dimensions. In Section 3, we show the way to extend the first order positivity-preserving Lagrangian schemes to high order schemes. In Section 4, one- and two-dimensional numerical examples are given to verify the performance of the new Lagrangian schemes. In Section 5 we will give concluding remarks.

2 First order positivity-preserving Lagrangian scheme solving the Euler equations with general EOS

2.1 The positivity-preserving HLLC approximate Riemann solver for the Lagrangian method

The Euler equations for unsteady compressible flow in the reference frame of a moving control volume can be expressed in integral form in the Cartesian coordinates as

$$\frac{d}{dt}\int_{\Omega(t)} \mathbf{U} d\Omega + \int_{\Gamma(t)} \mathbf{F}(\mathbf{U},\mathbf{n}) d\Gamma = 0 \tag{2.1}$$

where $\Omega(t)$ is the moving control volume enclosed by its boundary $\Gamma(t)$. The vector of the conserved variables $\mathbf{U}$ and the flux vector $\mathbf{F}$ are given by

$$\mathbf{U} = \begin{pmatrix} \rho \\ \rho\mathbf{u} \\ E \end{pmatrix}, \qquad \mathbf{F} = \begin{pmatrix} \rho(\mathbf{u}-\dot{\mathbf{x}})\cdot\mathbf{n} \\ \rho\mathbf{u}(\mathbf{u}-\dot{\mathbf{x}})\cdot\mathbf{n} + p\,\mathbf{n} \\ E(\mathbf{u}-\dot{\mathbf{x}})\cdot\mathbf{n} + p\mathbf{u}\cdot\mathbf{n} \end{pmatrix} \tag{2.2}$$

where ρ is density, $\mathbf{u}$ is velocity, $\mathbf{m} = \rho\mathbf{u}$ is momentum, E is total energy and p is pressure, $\dot{\mathbf{x}}$ is the velocity of the control volume boundary $\Gamma(t)$, and $\mathbf{n}$ denotes the unit outward normal to $\Gamma(t)$. The system (2.1) represents the conservation of mass, momentum and energy.

This paper focuses on solving the governing equations (2.1) in a Lagrangian framework, in which it is assumed that $\dot{\mathbf{x}} = \mathbf{u}$, and the vectors $\mathbf{U}$ and $\mathbf{F}$ then take the simpler form

$$\mathbf{U} = \begin{pmatrix} \rho \\ \rho\mathbf{u} \\ E \end{pmatrix}, \qquad \mathbf{F} = \begin{pmatrix} 0 \\ p\,\mathbf{n} \\ p\mathbf{u}\cdot\mathbf{n} \end{pmatrix}. \tag{2.3}$$

The set of equations is completed by the addition of an equation of state (EOS) with the following general form

$$p = p(\rho, e) \tag{2.4}$$

where $e = \frac{E}{\rho} - \frac{1}{2}|\mathbf{u}|^2$ is the specific internal energy. The sound speed for the fluid flow is $c = \sqrt{p_\rho|_s} = \sqrt{p_\rho + \frac{pp_e}{\rho^2}}$, and physically the quantity inside the square root should be positive. In this paper, we will consider several commonly used multi-material problems with general EOS. To be more specific, the following three types of general EOS are involved:

1) The ideal EOS for the perfect gas,

$$p = (\gamma - 1)\rho e, \quad c = \sqrt{\gamma \frac{p}{\rho}} \tag{2.5}$$

where γ is a constant representing the ratio of specific heat capacities of the fluid.

2) The stiffened EOS for water,

$$p = (\gamma - 1)\rho e - \gamma p_c, \quad c = \sqrt{\gamma \frac{p + p_c}{\rho}} \tag{2.6}$$

where γ has the same meaning as that in the ideal EOS and p_c is another positive constant.

3) The Jones-Wilkins-Lee (JWL) EOS for the detonation-products gas,

$$p = (\gamma - 1)\rho e + f(\rho), \quad c = \sqrt{\frac{\gamma p - f(\rho) + \rho f'(\rho)}{\rho}} \tag{2.7}$$

where

$$f(\rho) = A_1 \left(1 - \frac{\omega\rho}{R_1\rho_0}\right) e^{-\frac{R_1\rho_0}{\rho}} + A_2 \left(1 - \frac{\omega\rho}{R_2\rho_0}\right) e^{-\frac{R_2\rho_0}{\rho}}$$

with constants $A_1, A_2, \rho_0, R_1, R_2, \gamma$ which guarantee $0 \le \rho \le \rho_0$ and $f(\rho) \ge 0$.

Physically, the fluid flow has the positivity property for some variables such as density, internal energy, the quantity inside the square root to define the sound speed, and so on. For some fluid materials such as perfect gas and detonation-products gas, pressure is always positive as well. But pressure may not always be positive for some fluid flows such as water which is described by the stiffened EOS (2.6).

Consider the Lagrangian scheme for the Euler equations (2.1), (2.3) in the one-dimensional case. The spatial domain Ω is discretized into N computational cells $I_i = [x_{i-1/2}, x_{i+1/2}]$ of sizes $\Delta x_i = x_{i+1/2} - x_{i-1/2}$ with $i = 1, \ldots, N$. For a given cell I_i, the location of the cell center is denoted by x_i. The fluid velocity $u_{i+1/2}$ is defined at the vertex of the mesh. All

the conserved variables are stored at the cell center x_i in the form of cell averages and this cell is their common control volume. For example, the values of the cell averages for the cell I_i, denoted by $\overline{\rho}_i$, $\overline{m}_i$ and $\overline{E}_i$, are defined as follows

$$\overline{\rho}_i = \frac{1}{\Delta x_i}\int_{I_i} \rho dx, \quad \overline{m}_i = \frac{1}{\Delta x_i}\int_{I_i} \rho u dx, \quad \overline{E}_i = \frac{1}{\Delta x_i}\int_{I_i} E dx.$$

The finite volume Lagrangian scheme with Euler forward time discretization for the governing equations (2.1), (2.3) in the one-dimensional case has the following form,

$$\overline{\mathbf{U}}_i^{n+1}\Delta x_i^{n+1} - \overline{\mathbf{U}}_i^{n}\Delta x_i^{n} = -\Delta t[\hat{\mathbf{F}}(\mathbf{U}_{i+1/2}^{-}, \mathbf{U}_{i+1/2}^{+}) - \hat{\mathbf{F}}(\mathbf{U}_{i-1/2}^{-}, \mathbf{U}_{i-1/2}^{+})], \tag{2.8}$$

$$\overline{\mathbf{U}} = \begin{pmatrix} \overline{\rho} \\ \overline{m} \\ \overline{E} \end{pmatrix}, \qquad \hat{\mathbf{F}} = \begin{pmatrix} \hat{f}_D \\ \hat{f}_m \\ \hat{f}_E \end{pmatrix} \tag{2.9}$$

where $\overline{\mathbf{U}}^n$, $\overline{\mathbf{U}}^{n+1}$ are the vectors of cell averages of the conserved variables and Δx^n, Δx^{n+1} are the lengths of the corresponding cell at the n-th and $(n+1)$-th time steps respectively. $\mathbf{U}_{i\pm1/2}^{\pm}$ are the values of the conserved variables at the left and right sides of the cell boundary $x_{i\pm1/2}$ respectively. For a high order spatial approximation, $\mathbf{U}_{i\pm1/2}^{\pm}$ are obtained from a high order reconstruction which will be discussed in the next section. $\hat{\mathbf{F}}$ is the vector of the numerical fluxes of mass, momentum and total energy across the cell boundary of its control volume $I_i(t)$ respectively.

For the first order spatial approximation, $\mathbf{U}_{i\pm1/2}^{\pm}$ are taken as the vectors of the cell averages of the conserved variables, that is, the scheme (2.8) becomes

$$\overline{\mathbf{U}}_i^{n+1}\Delta x_i^{n+1} = \overline{\mathbf{U}}_i^{n}\Delta x_i^{n} - \Delta t[\hat{\mathbf{F}}(\overline{\mathbf{U}}_i^{n}, \overline{\mathbf{U}}_{i+1}^{n}) - \hat{\mathbf{F}}(\overline{\mathbf{U}}_{i-1}^{n}, \overline{\mathbf{U}}_i^{n})]. \tag{2.10}$$

We define the Godunov-type intercell numerical flux as

$$\hat{\mathbf{F}}(\mathbf{U}^-, \mathbf{U}^+) = \mathbf{F}(\mathbf{U}^*)$$

where $\mathbf{U}^*$ is the similarity solution $\mathbf{U}(x/t)$ of the following Riemann problem

$$\begin{cases} \mathbf{U}_t + \mathbf{F}(\mathbf{U})_x = 0 \\ \mathbf{U}(x,0) = \begin{cases} \mathbf{U}^-, & x < 0 \\ \mathbf{U}^+, & x \geq 0 \end{cases} \end{cases} \tag{2.11}$$

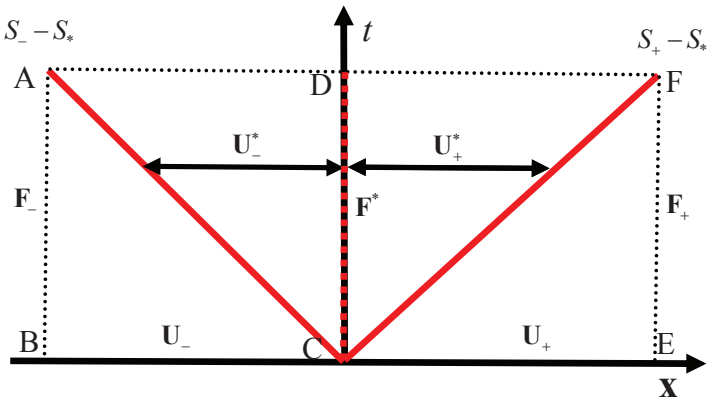

Figure 2.1: Simplified Riemann fan for the HLLC flux in the Lagrangian formulation.

evaluated along the contact wave in the Lagrangian formulation (see Figure 2.1) where

$$\mathbf{U} = \begin{pmatrix} \rho \\ \rho u \\ E \end{pmatrix}, \qquad \mathbf{F}(\mathbf{U}) = \begin{pmatrix} \rho(u - S_*) \\ \rho u(u - S_*) + p \\ E(u - S_*) + pu \end{pmatrix}. \tag{2.12}$$

$\mathbf{U}^{\pm} = (\rho_{\pm}, (\rho u)_{\pm}, E_{\pm})^T$. S_* denotes the velocity of the middle wave (the contact wave).

For the Euler equations, the solution to the Riemann problem consists of a contact wave and two acoustic waves, which may be either shocks or expansion fans. We denote the smallest and largest velocities of the acoustic waves as S_- and S_+ respectively.

Exact solution to the Riemann problem may be difficult and costly to obtain, hence often approximate Riemann solvers are used to build Godunov-type numerical schemes. In the approximate Riemann solvers for the Eulerian equations, the HLLC Riemann solver proposed and developed initially by Harten et al and further developed by Toro, Einfeldt et al [14, 28, 9] has been proved to be very simple, reliable and robust. It has been widely used in many application fields. In [1], Batten et al. further proved that the HLLC flux is positively conservative (for density and pressure) for the perfect gas in the Eulerian formulation with an appropriate choice of the acoustic wavespeeds. In this section, we will discuss the specific form of the HLLC flux for the Euler equations with general EOS in the Lagrangian formulation and prove that the scheme (2.10) based on this flux with suitably chosen wavespeeds S_- and S_+ is positivity-preserving.

For the HLLC flux, two averaged intermediate states $\mathbf{U}_-^*$ and $\mathbf{U}_+^*$ between the two acous-

tic waves S_-, S_+ are considered, which are separated by the contact wave (interface) with the velocity S_*. In the Lagrangian formulation we take the moving reference coordinate with the velocity of the contact wave S_* so that the contact wave is always at the position $x = 0$. Thus $\mathbf{F}(\mathbf{U}^*)$ would have the following form,

$$\mathbf{F}^* = \mathbf{F}(\mathbf{U}^*) = \begin{pmatrix} 0 \\ p^* \\ p^* S_* \end{pmatrix}$$

where p^* is the pressure along the contact wave which will be determined below. Figure 2.1 gives an illustration of the HLLC flux formulation in the Lagrangian framework.

Since the approximate Riemann solver does not give an exact solution to the Riemann problem, what we insist upon designing the HLLC flux is to enforce the divergence theorem. Integrating the Euler system (2.1) over the left and right halves of the Riemann fan, i.e. the rectangles ABCD and CEFD respectively in Figure 2.1, and enforcing the divergence theorem in each of them, we obtain the following expressions for the flux,

$$\mathbf{F}^*_- = \mathbf{F}_- + (S_- - S_*)(\mathbf{U}^*_- - \mathbf{U}_-) \tag{2.13}$$

$$\mathbf{F}^*_+ = \mathbf{F}_+ + (S_+ - S_*)(\mathbf{U}^*_+ - \mathbf{U}_+) \tag{2.14}$$

where $\mathbf{F}^*_\pm = \mathbf{F}(\mathbf{U}^*_\pm)$ and $\mathbf{F}_\pm = \mathbf{F}(\mathbf{U}_\pm)$ as defined by (2.12).

Equations (2.13)-(2.14) can be rewritten in details as follows,

$$\begin{aligned} & (S_- - S_*) \begin{bmatrix} \rho^*_- \\ \rho^*_- u^*_- \\ E^*_- \end{bmatrix} - \begin{bmatrix} \rho^*_-(u^*_- - S_*) \\ \rho^*_- u^*_-(u^*_- - S_*) + p^*_- \\ E^*_-(u^*_- - S_*) + p^*_- u^*_- \end{bmatrix} \\ = \quad & (S_- - S_*) \begin{bmatrix} \rho_- \\ \rho_- u_- \\ E_- \end{bmatrix} - \begin{bmatrix} \rho_-(u_- - S_*) \\ \rho_- u_-(u_- - S_*) + p_- \\ E_-(u_- - S_*) + p_- u_- \end{bmatrix} \end{aligned} \tag{2.15}$$

and

$$\begin{aligned} & (S_+ - S_*) \begin{bmatrix} \rho^*_+ \\ \rho^*_+ u^*_+ \\ E^*_+ \end{bmatrix} - \begin{bmatrix} \rho^*_+(u^*_+ - S_*) \\ \rho^*_+ u^*_+(u^*_+ - S_*) + p^*_+ \\ E^*_+(u^*_+ - S_*) + p^*_+ u^*_+ \end{bmatrix} \\ = \quad & (S_+ - S_*) \begin{bmatrix} \rho_+ \\ \rho_+ u_+ \\ E_+ \end{bmatrix} - \begin{bmatrix} \rho_+(u_+ - S_*) \\ \rho_+ u_+(u_+ - S_*) + p_+ \\ E_+(u_+ - S_*) + p_+ u_+ \end{bmatrix}. \end{aligned} \tag{2.16}$$

Using the fact that the left and right values of velocity and pressure along the contact wave are the same, that is,

$$\begin{cases} p^* = p_-^* = p_+^* \\ S_* = u_-^* = u_+^* \end{cases}, \tag{2.17}$$

we have $\mathbf{F}^* = \mathbf{F}_-^* = \mathbf{F}_+^*$. From the above expressions (2.15)-(2.16), we can get the following simple form of the HLLC flux in the Lagrangian formulation,

$$\hat{\mathbf{F}}(\mathbf{U}^-, \mathbf{U}^+) = \mathbf{F}^* = \begin{pmatrix} 0 \\ p^* \\ p^* S_* \end{pmatrix} \tag{2.18}$$

where

$$p^* = \rho_-(u_- - S_-)(u_- - S_*) + p_- \tag{2.19}$$

$$S_* = \frac{\rho_+ u_+(S_+ - u_+) - \rho_- u_-(S_- - u_-) + p_- - p_+}{\rho_+(S_+ - u_+) - \rho_-(S_- - u_-)} \tag{2.20}$$

and

$$\begin{cases} \rho_-^* = \rho_- \frac{S_- - u_-}{S_- - S_*} \\ \rho_-^* u_-^* = \frac{(S_- - u_-)\rho_- u_- + (p^* - p_-)}{S_- - S_*} \\ E_-^* = \frac{(S_- - u_-)E_- - p_- u_- + p^* S_*}{S_- - S_*} \end{cases}. \tag{2.21}$$

Similar expression can be obtained for $\mathbf{U}_+^*$. The acoustic wavespeeds S_- and S_+ will be determined later to make the Lagrangian scheme positivity-preserving.

Define the set of admissible states by

$$G = \left\{ \mathbf{U} = \begin{bmatrix} \rho \\ \rho u \\ E \end{bmatrix}, \quad \rho > 0, \quad e = E/\rho - \frac{1}{2}|u|^2 > 0, \quad c^2 = p_\rho|_s > 0 \right\}. \tag{2.22}$$

Lemma: The set of admissible states G is a convex set for the previous mentioned three types of EOS given by (2.5)-(2.7).

Proof. From the expressions (2.5)-(2.7), we can easily verify:

1) For the ideal EOS, if $\rho > 0$, then $e > 0 \Longleftrightarrow c^2 > 0$.

2) For the stiffened EOS, if $\rho > 0$, then $\rho e - p_c > 0 \Longleftrightarrow c^2 > 0$.

3) For the JWL EOS, if $\rho > 0$, then $e > 0 \Longrightarrow c^2 > 0$.

Thus for the ideal EOS and the JWL EOS, G can be described as

$$G = \left\{ \mathbf{U} = \begin{bmatrix} \rho \\ \rho u \\ E \end{bmatrix}, \quad \rho > 0, \quad e > 0 \right\}. \tag{2.23}$$

For the stiffened EOS, G can be described as

$$G = \left\{ \mathbf{U} = \begin{bmatrix} \rho \\ \rho u \\ E \end{bmatrix}, \quad \rho > 0, \quad \rho e - p_c > 0 \right\}. \tag{2.24}$$

Denote $\breve{e} = \rho e, \tilde{e} = \rho e - p_c$. Since ρe is a concave function of $\mathbf{U}$, using Jensen's inequality, we have

$$\breve{e}(a\mathbf{U}_1 + (1-a)\mathbf{U}_2) \geq a\breve{e}(\mathbf{U}_1) + (1-a)\breve{e}(\mathbf{U}_2), \quad if \quad \rho_1 \geq 0, \quad \rho_2 \geq 0,$$

$$\tilde{e}(a\mathbf{U}_1 + (1-a)\mathbf{U}_2) \geq a\tilde{e}(\mathbf{U}_1) + (1-a)\tilde{e}(\mathbf{U}_2), \quad if \quad \rho_1 \geq 0, \quad \rho_2 \geq 0,$$

for $\mathbf{U}_1 = (\rho_1, m_1, E_1)$, $\mathbf{U}_2 = (\rho_2, m_2, E_2)$ and $0 \leq a \leq 1$. Thus G is a convex set.

The scheme (2.10) is called positivity-preserving if $\{\overline{\mathbf{U}}_i^n \in G, i = 1, ..., N\}$ implies $\{\overline{\mathbf{U}}_i^{n+1} \in G, i = 1, ..., N\}$. Following the design of the HLLC flux, under a suitable CFL condition, the two waves in Figure 2.2 centered at $x_{i-1/2}$ and at $x_{i+1/2}$ do not interact within the time step Δt, and divergence theorem is satisfied exactly in the two rectangles ABCD and CEFD respectively in Figure 2.1. With also the continuity of p^* at the contact (the line CD in Figure 2.1), $\overline{\mathbf{U}}_i^{n+1}$ in the scheme (2.10) can be described as the exact integration of the approximate Riemann solver over $[x_{i-1/2}^{n+1}, x_{i+1/2}^{n+1}]$ broken into two pieces (see Figure 2.2), that is,

$$\overline{\mathbf{U}}_i^{n+1} = \frac{1}{\Delta x_i^{n+1}} \int_{x_{i-1/2}^{n+1}}^{x_i^{n+1}} R(x/t, \overline{\mathbf{U}}_{i-1}^n, \overline{\mathbf{U}}_i^n) dx + \frac{1}{\Delta x_i^{n+1}} \int_{x_i^{n+1}}^{x_{i+1/2}^{n+1}} R(x/t, \overline{\mathbf{U}}_i^n, \overline{\mathbf{U}}_{i+1}^n) dx \tag{2.25}$$

where $R(x/t, \overline{\mathbf{U}}_{j-1}^n, \overline{\mathbf{U}}_j^n)$ (for $j = i$ and $j = i+1$) is the approximate Riemann solution between the states $\overline{\mathbf{U}}_{j-1}^n$ and $\overline{\mathbf{U}}_j^n$. To be more specific, for the HLLC Riemann solver, $R(x/t, \overline{\mathbf{U}}_{i-1}^n, \overline{\mathbf{U}}_i^n)$ in the relevant integration interval will take the value of either $\mathbf{U}_+^*$ (computed from the two states $\overline{\mathbf{U}}_{i-1}^n$ and $\overline{\mathbf{U}}_i^n$) or $\overline{\mathbf{U}}_i^n$. Similarly $R(x/t, \overline{\mathbf{U}}_i^n, \overline{\mathbf{U}}_{i+1}^n)$ in the relevant

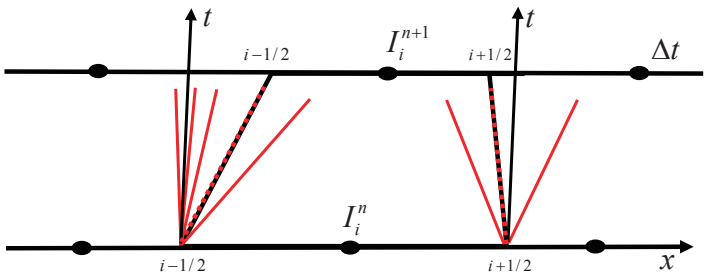

Figure 2.2: Illustration of the Lagrangian scheme with the approximate Riemann solver.

integration interval will take the value of either $\overline{\mathbf{U}}_i^n$ or $\mathbf{U}_-^*$ (computed from the two states $\overline{\mathbf{U}}_i^n$ and $\overline{\mathbf{U}}_{i+1}^n$). Thus in order to prove the positivity-preserving property of the scheme (2.10), we only need to prove the intermediate states $\mathbf{U}_\pm^* \in G$ if $\mathbf{U}_\pm \in G$, which would imply that $\overline{\mathbf{U}}_i^{n+1}$ given by (2.25) also belongs to G, due to the fact that G is a convex set and Jensen's inequality for integrals. According to the definition of G in (2.23) for the ideal EOS and the JWL EOS, we need to prove if

$$\begin{cases} \rho_- > 0, & E_- - \frac{1}{2}\rho_- u_-^2 > 0 \\ \rho_+ > 0, & E_+ - \frac{1}{2}\rho_+ u_+^2 > 0 \end{cases}, \tag{2.26}$$

then

$$\rho_-^* > 0, \qquad \rho_+^* > 0, \tag{2.27}$$

$$E_-^* - \frac{1}{2}\rho_-^*(u_-^*)^2 > 0, \quad E_+^* - \frac{1}{2}\rho_+^*(u_+^*)^2 > 0. \tag{2.28}$$

For simplicity, we only give the proof for the validity of (2.27)-(2.28) for $\mathbf{U}_-^*$. Similar arguments can prove the validity for $\mathbf{U}_+^*$ as well.

Since $S_- < S_*$, $S_- < u_-$, the inequality (2.27) is easily obtained from (2.21). By using (2.21), the inequality (2.28) can be rewritten as

$$(u_- - S_-)E_- + p_- u_- - p^* S_* + \frac{((S_- - u_-)\rho_- u_- - p_- + p^*)^2}{2\rho_-(S_- - u_-)} > 0. \tag{2.29}$$

Substituting the expression (2.19) into (2.29) and rearranging, we have

$$(u_- - S_-)[E_- - \rho_-(u_- - S_*)S_* - \frac{1}{2}\rho_- S_*^2] + (u_- - S_*)p_- > 0. \tag{2.30}$$

Using the relationship $E_- = \rho_- e_- + \frac{1}{2}\rho_- u_-^2$, the inequality (2.30) becomes

$$\frac{1}{2}\rho_-(S_* - u_-)^2 - \frac{p_-}{u_- - S_-}(S_* - u_-) + \rho_- e_- > 0. \tag{2.31}$$

Defining $\xi = S_* - u_-$, we finally get the inequality to verify as

$$\frac{1}{2}\rho_-\xi^2 - \frac{p_-}{u_- - S_-}\xi + \rho_- e_- > 0. \tag{2.32}$$

To guarantee the inequality (2.32) to hold for any value of ξ, the discriminant of the quadratic function of ξ on the left side of (2.32) should be negative, which gives the following condition for the acoustic wavespeed S_-,

$$\frac{p_-^2}{(u_- - S_-)^2} - 2\rho_-^2 e_- < 0, \tag{2.33}$$

that is,

$$S_- < u_- - \frac{p_-}{\rho_-\sqrt{2e_-}}. \tag{2.34}$$

By a similar derivation, we can get the condition for the acoustic wavespeed S_+,

$$S_+ > u_+ + \frac{p_+}{\rho_+\sqrt{2e_+}}. \tag{2.35}$$

For Euler equations with the stiffened EOS in which the definition of G is described by (2.24), by a similar argument, we can prove that $\mathbf{U}_\pm^* \in G$ if $\mathbf{U}_\pm \in G$ under the following condition

$$S_- < u_- - \frac{p_- + p_c}{\sqrt{2\rho_-(\rho_- e_- - p_c)}}, \quad S_+ > u_+ + \frac{p_+ + p_c}{\sqrt{2\rho_+(\rho_+ e_+ - p_c)}}. \tag{2.36}$$

In particular, for the ideal EOS, from (2.5), we have $\frac{p}{\rho\sqrt{2e}} = \sqrt{\frac{(\gamma-1)p}{2\rho}} < \sqrt{\frac{\gamma p}{\rho}} = c$. For the stiffened EOS, using (2.6), we get $\frac{p+p_c}{\sqrt{2\rho(\rho e - p_c)}} = \sqrt{\frac{(\gamma-1)(p+p_c)}{2\rho}} < \sqrt{\frac{\gamma(p+p_c)}{\rho}} = c$. Thus the final acoustic wavespeeds S_- and S_+ can be taken as follows,

$$S_- = \min\left[u_- - \frac{p_-}{\rho_-\sqrt{2e_-}}, u_- - c_-, \tilde{u} - \tilde{c}\right], \quad S_+ = \max\left[u_+ + \frac{p_+}{\rho_+\sqrt{2e_+}}, u_+ + c_+, \tilde{u} + \tilde{c}\right] \tag{2.37}$$

where $\tilde{u}$, $\tilde{c}$ are the Roe's averages of the fluid velocity and sound speed respectively.

For the ideal EOS and stiffened EOS, S_- and S_+ in (2.37) have the same simpler forms as those in [9] which can yield the exact velocity for isolated shocks,

$$S_- = \min[u_- - c_-, \tilde{u} - \tilde{c}], \qquad S_+ = \max[u_+ + c_+, \tilde{u} + \tilde{c}]. \tag{2.38}$$

In summary, we have the following theorem for the scheme (2.10).

Theorem 2.1. *Consider the finite volume Lagrangian scheme (2.10) with the HLLC flux (2.18)-(2.20) solving the Euler equations (2.1), (2.3) with the general equation of state given by one of (2.5)-(2.7). If* $\{\overline{\boldsymbol{U}}_i^n \in G, \forall i = 1, ..., N\}$*, then the scheme is positivity-preserving, namely,* $\{\overline{\boldsymbol{U}}_i^{n+1} \in G, \forall i = 1, ..., N\}$ *under the choice of the acoustic wavespeeds* S_- *and* S_+ *in (2.37) and with the time step restriction*

$$\Delta t^n \leq \lambda \min_{i=1,...,N} \left(\Delta x_i^n \Big/ \left(\max \left\{ \left| \frac{p_i^n}{\rho_i^n \sqrt{2e_i^n}} \right|, c_i^n \right\} + |u_i^n| \right) \right) \tag{2.39}$$

with the Courant number $\lambda = 1/2$.

Remark 2.1. *The time step restriction (2.39) with the Courant number* $\lambda = 1/2$ *is used to guarantee that the two waves in Figure 2.2 centered at* $x_{i-1/2}$ *and at* $x_{i+1/2}$ *do not interact within the time step* Δt.

Remark 2.2. *If* G *is described as (2.23), then Theorem 2.1 holds for the Euler equations (2.1), (2.3) with any EOS.*

As to the vertex velocity $u_{i+1/2}$ which is used to determine the motion of the grid, it is simply taken as S_* solved by (2.20) at the corresponding point. After we get the velocity at each cell vertex, the cell vertex moves with the following discretized local kinematic equation

$$x_{i+1/2}^{n+1} = x_{i+1/2}^n + \Delta t^n u_{i+1/2}^n$$

where $u_{i+1/2}^n$ is the vertex velocity at the n-th time step, $x_{i+1/2}^n, x_{i+1/2}^{n+1}$ are the vertex position at the n-th and $(n+1)$-th time steps respectively.

2.2 The first order positivity-preserving Lagrangian scheme in the two-dimensional space

The 2D spatial domain Ω is discretized into $M \times N$ computational cells. $I_{i,j}$ is a quadrilateral cell constructed by the four vertices $\{(x_{i-1/2,j-1/2}, y_{i-1/2,j-1/2}), (x_{i+1/2,j-1/2}, y_{i+1/2,j-1/2}), (x_{i+1/2,j+1/2}, y_{i+1/2,j+1/2}), (x_{i-1/2,j+1/2}, y_{i-1/2,j+1/2})\}$. $A_{i,j}$ is used to denote the area of the cell $I_{i,j}$ with $i = 1, \ldots, M$, $j = 1, \ldots, N$. The values of the cell averages for the cell $I_{i,j}$ denoted by $\overline{\rho}_{i,j}$, $\overline{\mathbf{m}}_{i,j}$, and $\overline{E}_{i,j}$ are defined as follows

$$\overline{\rho}_{i,j} = \frac{1}{A_{i,j}} \iint_{I_{i,j}} \rho dxdy, \quad \overline{\mathbf{m}}_{i,j} = \frac{1}{A_{i,j}} \iint_{I_{i,j}} \rho \mathbf{u} dxdy, \quad \overline{E}_{i,j} = \frac{1}{A_{i,j}} \iint_{I_{i,j}} E dxdy.$$

The conservative Lagrangian scheme for the Euler equations (2.1), (2.3) has the following form in the two-dimensional space

$$\overline{\mathbf{U}}_{i,j}^{n+1} A_{i,j}^{n+1} - \overline{\mathbf{U}}_{i,j}^{n} A_{i,j}^{n} = -\Delta t \int_{\partial I_{i,j}} \hat{\mathbf{F}}(\mathbf{U}^{int(I_{i,j})}, \mathbf{U}^{ext(I_{i,j})}, \mathbf{n}_{I_{i,j}}) dl, \tag{2.40}$$

$$\overline{\mathbf{U}}_{i,j} = \begin{pmatrix} \overline{\rho}_{i,j} \\ \overline{\mathbf{m}}_{i,j} \\ \overline{E}_{i,j} \end{pmatrix}, \quad \hat{\mathbf{F}} = \begin{pmatrix} \hat{f}_D \\ \hat{f}_{\mathbf{m}} \\ \hat{f}_E \end{pmatrix} \tag{2.41}$$

where the variables with the superscript n and $n+1$ represent the values of the corresponding variables at the n-th and $(n+1)$-th time steps respectively. $\mathbf{U}^{int(I_{i,j})} = (\rho^{int(I_{i,j})}, \mathbf{m}^{int(I_{i,j})}, E^{int(I_{i,j})})^T$ and $\mathbf{U}^{ext(I_{i,j})} = (\rho^{ext(I_{i,j})}, \mathbf{m}^{ext(I_{i,j})}, E^{ext(I_{i,j})})^T$ are the vectors of the conserved variables inside the cell $I_{i,j}$ and outside the cell $I_{i,j}$ (inside the neighboring cell) at the cell boundary $\partial I_{i,j}$ respectively. $\hat{\mathbf{F}}$ is the vector of the numerical fluxes for mass, momentum and total energy across the cell boundary $\partial I_{i,j}$. $\mathbf{n}_{I_{i,j}} = (n_x, n_y)$ is the unit outward normal to the quadrilateral cell boundary. For simplicity, we omit the superscript 'n' for all the variables which appear at the right side of the scheme (2.40). The numerical flux satisfies $\hat{\mathbf{F}}(\mathbf{U}, \mathbf{U}, \mathbf{n}) = \mathbf{F}(\mathbf{U}, \mathbf{n}) = (0, p\mathbf{n}, p\mathbf{u} \cdot \mathbf{n})^T$ for consistency and $\hat{\mathbf{F}}(\mathbf{U}, \mathbf{V}, \mathbf{n}) = -\hat{\mathbf{F}}(\mathbf{V}, \mathbf{U}, -\mathbf{n})$ for conservation.

If the line integral in Eq. (2.40) is discretized by a K-point Gaussian integration formula

for each edge, then we have

$$\int_{\partial I_{i,j}} \hat{\mathbf{F}} dl \approx \sum_{m=1}^{M} \sum_{\alpha=1}^{K} \omega_\alpha \hat{\mathbf{F}}(\mathbf{U}_{m,\alpha}^{int(I_{i,j})}, \mathbf{U}_{m,\alpha}^{ext(I_{i,j})}, \mathbf{n}_{I_{i,j}}^m) l_{i,j}^m \tag{2.42}$$

where the terms at the right hand side represent the line integral of the numerical flux along the boundary edges of the cell $I_{i,j}$. M is the number of the cell boundary edges, for the quadrilateral grid $M = 4$. $\mathbf{n}_{I_{i,j}}^m$ is the unit outward normal of $I_{i,j}$ along the m-th cell edge. $l_{i,j}^m$ is the length of the m-th edge of the cell boundary for the cell $I_{i,j}$. $\{\mathbf{U}_{m,\alpha}^{int(I_{i,j})}, \mathbf{U}_{m,\alpha}^{ext(I_{i,j})}, \alpha = 1, ..., K\}$ are the values of the reconstruction polynomial $\mathbf{U}$ at the Gaussian quadrature points inside and outside the cell $I_{i,j}$ along the m-th cell edge respectively.

In a similar way as introduced in the last section, we can get the HLLC numerical flux for the Euler equations in two spatial dimensions

$$\hat{\mathbf{F}}(\mathbf{U}^{int}, \mathbf{U}^{ext}, \mathbf{n}) = \begin{pmatrix} 0 \\ p^* n_x \\ p^* n_y \\ p^* S_* \end{pmatrix} \tag{2.43}$$

where

$$\begin{aligned} p^* &= \rho^{int}(u_n^{int} - S_-)(u_n^{int} - S_*) + p^{int}, \\ S_* &= \frac{\rho^{ext} u_n^{ext}(S_+ - u_n^{ext}) - \rho^{int} u_n^{int}(S_- - u_n^{int}) + p^{int} - p^{ext}}{\rho^{ext}(S_+ - u_n^{ext}) - \rho^{int}(S_- - u_n^{int})}, \\ S_- &= \min\left[u_n^{int} - \frac{p^{int}}{\rho^{int}\sqrt{2e^{int}}}, u_n^{int} - c^{int}, \tilde{u}_n - \tilde{c}\right], \\ S_+ &= \max\left[u_n^{ext} + \frac{p^{ext}}{\rho^{ext}\sqrt{2e^{ext}}}, u_n^{ext} + c^{ext}, \tilde{u}_n + \tilde{c}\right] \end{aligned} \tag{2.44}$$

with $u_n^{int} = \mathbf{m}^{int} \cdot \mathbf{n}/\rho^{int}$, $u_n^{ext} = \mathbf{m}^{ext} \cdot \mathbf{n}/\rho^{ext}$. $\tilde{u}_n$ and $\tilde{c}$ are the Roe averages of u_n and c respectively.

For the first order scheme, $\mathbf{U}^{int}$ and $\mathbf{U}^{ext}$ in (2.42) are taken as the values of the cell averages for the conserved variables at the inside and outside cells along the cell edge. The line integral of $\hat{\mathbf{F}}$ along each cell edge can simply be calculated by the middle-point integration formula. Thus the first order Lagrangian scheme in the two-dimensional space can be written

in the following form,

$$\overline{\mathbf{U}}_{i,j}^{n+1} A_{i,j}^{n+1} \;=\; \overline{\mathbf{U}}_{i,j}^{n} A_{i,j}^{n} - \Delta t \sum_{m=1}^{M} \hat{\mathbf{F}}(\overline{\mathbf{U}}_{i,j}^{n}, \overline{\mathbf{U}}_{m}^{ext(I_{i,j})}, \mathbf{n}_{I_{i,j}}^{m}) l_{i,j}^{m} \tag{2.45}$$

where $\overline{\mathbf{U}}_{m}^{ext(I_{i,j})}$ is the cell average of $\mathbf{U}$ in the neighboring cell of $I_{i,j}$ along the m-th cell edge.

By (2.2), we clearly have $\mathbf{F}(\mathbf{U}, \mathbf{n}) = \tilde{\mathbf{F}}(\mathbf{U}) \cdot \mathbf{n}$ for a vector flux $\tilde{\mathbf{F}}(\mathbf{U})$. Also geometrically it is clear that $\sum_{m=1}^{M} \mathbf{n}_{I_{i,j}}^{m} l_{i,j}^{m} = 0$. Therefore, by the consistency of numerical fluxes, we have

$$\sum_{m=1}^{M} \hat{\mathbf{F}}(\overline{\mathbf{U}}_{i,j}^{n}, \overline{\mathbf{U}}_{i,j}^{n}, \mathbf{n}_{I_{i,j}}^{m}) l_{i,j}^{m} = \sum_{m=1}^{M} \mathbf{F}(\overline{\mathbf{U}}_{i,j}^{n}, \mathbf{n}_{I_{i,j}}^{m}) l_{i,j}^{m} = \tilde{\mathbf{F}}(\overline{\mathbf{U}}_{i,j}^{n}) \sum_{m=1}^{M} \mathbf{n}_{I_{i,j}}^{m} l_{i,j}^{m} = 0.$$

By adding $0 = \Delta t \sum_{m=1}^{M} \hat{\mathbf{F}}(\overline{\mathbf{U}}_{i,j}^{n}, \overline{\mathbf{U}}_{i,j}^{n}, \mathbf{n}_{I_{i,j}}^{m}) l_{i,j}^{m}$ to the scheme (2.45), we have

$$\begin{aligned}
\overline{\mathbf{U}}_{i,j}^{n+1} A_{i,j}^{n+1} &= \overline{\mathbf{U}}_{i,j}^{n} A_{i,j}^{n} - \Delta t \sum_{m=1}^{M} [\hat{\mathbf{F}}(\overline{\mathbf{U}}_{i,j}^{n}, \overline{\mathbf{U}}_{m}^{ext(I_{i,j})}, \mathbf{n}_{I_{i,j}}^{m}) - \hat{\mathbf{F}}(\overline{\mathbf{U}}_{i,j}^{n}, \overline{\mathbf{U}}_{i,j}^{n}, \mathbf{n}_{I_{i,j}}^{m})] l_{i,j}^{m} \\
&= \sum_{m=1}^{M} \left\{ \frac{A_{i,j}^{n}}{\sum_{m=1}^{M} l_{i,j}^{m}} \overline{\mathbf{U}}_{i,j}^{n} - \Delta t \left[\hat{\mathbf{F}}(\overline{\mathbf{U}}_{i,j}^{n}, \overline{\mathbf{U}}_{m}^{ext(I_{i,j})}, \mathbf{n}_{I_{i,j}}^{m}) - \hat{\mathbf{F}}(\overline{\mathbf{U}}_{i,j}^{n}, \overline{\mathbf{U}}_{i,j}^{n}, \mathbf{n}_{I_{i,j}}^{m}) \right] \right\} l_{i,j}^{m}.
\end{aligned}$$

Define

$$\hat{\mathcal{F}}^{m} = \frac{A_{i,j}^{n}}{\sum_{m=1}^{M} l_{i,j}^{m}} \overline{\mathbf{U}}_{i,j}^{n} - \Delta t \left[\hat{\mathbf{F}}(\overline{\mathbf{U}}_{i,j}^{n}, \overline{\mathbf{U}}_{m}^{ext(I_{i,j})}, \mathbf{n}_{I_{i,j}}^{m}) - \hat{\mathbf{F}}(\overline{\mathbf{U}}_{i,j}^{n}, \overline{\mathbf{U}}_{i,j}^{n}, \mathbf{n}_{I_{i,j}}^{m}) \right]. \tag{2.46}$$

Clearly, $\hat{\mathcal{F}}^{m}$ is a formal one-dimensional first order positivity-preserving scheme, namely, the same type as (2.10). The only difference between them is the former vector $\overline{\mathbf{U}}$ has four components while the latter one in the one-dimensional case (2.10) has only three components. This additional component corresponds to the linear degenerate contact discontinuity field and is a simple shear term, a similar proof as in the one-dimensional case can lead to the proof that $\hat{\mathcal{F}}^{m}$ is also in the set G under the CFL condition

$$\Delta t^{n} \leq \lambda \min_{i,j} \left\{ \frac{A_{i,j}^{n}}{\sum_{m=1}^{M} l_{i,j}^{m}} \Bigg/ \left(\max \left\{ \left| \frac{p_{i,j}^{n}}{\rho_{i,j}^{n} \sqrt{2 e_{i,j}^{n}}} \right|, c_{i,j}^{n} \right\} + |\mathbf{u}_{i,j}^{n}| \right) \right\} \tag{2.47}$$

where $c_{i,j}^{n}$ is the sound speed within this cell. The Courant number $\lambda = 1/2$ is the same as in the one-dimensional case. Since $\overline{\mathbf{U}}^{n+1}$ is a convex combination of $\hat{\mathcal{F}}^{m}$, the following theorem is obtained by using the fact that G is a convex set.

Theorem 2.2. *Consider the first order Lagrangian scheme (2.45) with the HLLC flux (2.43)-(2.44) solving the Euler equations (2.1), (2.3) with the general equation of state given by one of (2.5)-(2.7). The scheme (2.45) is positivity-preserving, namely,* $\{\overline{\boldsymbol{U}}_{i,j}^{n+1} \in G, \forall i = 1, ..., M, j = 1, ..., N\}$ *if* $\{\overline{\boldsymbol{U}}_{i,j}^{n} \in G, \forall i = 1, ..., M, j = 1, ..., N\}$ *under the time step restriction (2.47) with* $\lambda = 1/2$.

The vertex velocity for the motion of the grid is determined in a similar way as that in [5]. Briefly, we first obtain the tangential and normal velocities along each edge connected to the vertex. Specifically, the tangential velocity of the vertex (or edge center) along the edge is defined as a simple average of that on both sides. The normal velocity along each edge connected to the vertex is taken as S_*. Finally the velocity of the vertex is set to be the arithmetic average of the velocities along the edges sharing this vertex.

3 High order positivity-preserving Lagrangian scheme for the Euler equations with general EOS

3.1 High order positivity-preserving Lagrangian scheme in the one-dimensional space

We first consider a general high-order finite volume Lagrangian scheme in the one-dimensional space which has the form (2.8). To obtain high order accurate spatial discretization for the scheme (2.8), by the information of the corresponding cell-average conserved variables from the cell I_i and its neighboring cells, a polynomial vector $\{\mathbf{U}_i(x) = (\rho_i(x), m_i(x), E_i(x))^T$ is obtained by applying the techniques of the ENO reconstruction and local characteristic decomposition. $\{\mathbf{U}_{i\pm1/2}^{\pm}, i = 1, ..., N\}$ is then determined by $\{\mathbf{U}_i(x), i = 1, ..., N\}$. We refer to our previous work [5, 6] for the details.

Assume a polynomial vector $\mathbf{U}_i(x)$ is obtained by the ENO reconstruction with degree k, where $k \geq 1$, defined on I_i such that $\overline{\mathbf{U}}_i^n$ is the cell average of $\mathbf{U}_i(x)$ on I_i, $\mathbf{U}_{i+\frac{1}{2}}^{-} = \mathbf{U}_i(x_{i+\frac{1}{2}})$, $\mathbf{U}_{i-\frac{1}{2}}^{+} = \mathbf{U}_i(x_{i-\frac{1}{2}})$.

Consider the K-point Legendre Gauss-Lobatto quadrature rule on the interval I_i which

is exact for the integral of polynomials of degree up to $2K-3$. We denote these quadrature points on I_i as

$$S_i = \{x_{i-\frac{1}{2}} = \hat{x}_i^1, \hat{x}_i^2, ..., \hat{x}_i^{K-1}, \hat{x}_i^K = x_{i+\frac{1}{2}}\}.$$

Define ω^α to be the quadrature weights such that $\omega_\alpha \geq 0, \alpha = 1, ..., K$ and $\sum_{\alpha=1}^K \omega_\alpha = 1$. Next, we will show that a sufficient condition for the scheme (2.8) to satisfy $\overline{\mathbf{U}}_i^{n+1} \in G$ is that $\mathbf{U}_i(\hat{x}_i^\alpha) \in G$ for all i and α, under a suitable CFL condition.

If we choose K to be the smallest integer satisfying $2K-3 \geq k$, then the K-point Legendre Gauss-Lobatto rule is exact for the polynomial $\mathbf{U}_i(x)$, which implies

$$\overline{\mathbf{U}}_i^n = \frac{1}{\Delta x_i}\int_{x_{i-\frac{1}{2}}}^{x_{i+\frac{1}{2}}} \mathbf{U}_i(x)dx = \sum_{\alpha=1}^K \omega_\alpha \mathbf{U}_i(\hat{x}_i^\alpha) = \sum_{\alpha=2}^{K-1} \omega_\alpha \mathbf{U}_i^\alpha + \omega_1 \mathbf{U}_{i-1/2}^+ + \omega_K \mathbf{U}_{i+1/2}^- \qquad (3.1)$$

where $\mathbf{U}_i^\alpha = \mathbf{U}_i(\hat{x}_i^\alpha)$.

By adding and subtracting $\Delta t \hat{\mathbf{F}}(\mathbf{U}_{i-1/2}^+, \mathbf{U}_{i+1/2}^-)$, the scheme (2.8) becomes

$$\begin{aligned}
\overline{\mathbf{U}}_i^{n+1}\Delta x_i^{n+1} &= \sum_{\alpha=1}^K \omega_\alpha \mathbf{U}_i^\alpha \Delta x_i^n \\
&\quad -\Delta t[\hat{\mathbf{F}}(\mathbf{U}_{i+\frac{1}{2}}^-, \mathbf{U}_{i+\frac{1}{2}}^+) - \hat{\mathbf{F}}(\mathbf{U}_{i-\frac{1}{2}}^+, \mathbf{U}_{i+\frac{1}{2}}^-) + \hat{\mathbf{F}}(\mathbf{U}_{i-\frac{1}{2}}^+, \mathbf{U}_{i+\frac{1}{2}}^-) - \hat{\mathbf{F}}(\mathbf{U}_{i-\frac{1}{2}}^-, \mathbf{U}_{i-\frac{1}{2}}^+)] \\
&= \sum_{\alpha=2}^{K-1} \omega_\alpha \mathbf{U}_i^\alpha \Delta x_i^n \\
&\quad +\omega_K\{\mathbf{U}_{i+\frac{1}{2}}^- \Delta x_i^n - \frac{\Delta t}{\omega_K}[\hat{\mathbf{F}}(\mathbf{U}_{i+\frac{1}{2}}^-, \mathbf{U}_{i+\frac{1}{2}}^+) - \hat{\mathbf{F}}(\mathbf{U}_{i-\frac{1}{2}}^+, \mathbf{U}_{i+\frac{1}{2}}^-)]\} \\
&\quad +\omega_1\{\mathbf{U}_{i-\frac{1}{2}}^+ \Delta x_i^n - \frac{\Delta t}{\omega_1}[\hat{\mathbf{F}}(\mathbf{U}_{i-\frac{1}{2}}^+, \mathbf{U}_{i+\frac{1}{2}}^-) - \hat{\mathbf{F}}(\mathbf{U}_{i-\frac{1}{2}}^-, \mathbf{U}_{i-\frac{1}{2}}^+)]\} \\
&= \sum_{\alpha=2}^{K-1} \omega_\alpha \mathbf{U}_i^\alpha \Delta x_i^n + \omega_K \hat{\mathcal{F}}_K + \omega_1 \hat{\mathcal{F}}_1
\end{aligned}$$

where

$$\hat{\mathcal{F}}_1 = \mathbf{U}_{i-\frac{1}{2}}^+ \Delta x_i^n - \frac{\Delta t}{\omega_1}[\hat{\mathbf{F}}(\mathbf{U}_{i-\frac{1}{2}}^+, \mathbf{U}_{i+\frac{1}{2}}^-) - \hat{\mathbf{F}}(\mathbf{U}_{i-\frac{1}{2}}^-, \mathbf{U}_{i-\frac{1}{2}}^+)], \qquad (3.2)$$

$$\hat{\mathcal{F}}_K = \mathbf{U}_{i+\frac{1}{2}}^- \Delta x_i^n - \frac{\Delta t}{\omega_K}[\hat{\mathbf{F}}(\mathbf{U}_{i+\frac{1}{2}}^-, \mathbf{U}_{i+\frac{1}{2}}^+) - \hat{\mathbf{F}}(\mathbf{U}_{i-\frac{1}{2}}^+, \mathbf{U}_{i+\frac{1}{2}}^-)]. \qquad (3.3)$$

Notice that (3.2) and (3.3) are both of the type (2.10), and $\omega_1 = \omega_K$. Therefore if $\hat{\mathbf{F}}$ is determined by the HLLC numerical flux (2.18)-(2.20) with the acoustic wavespeeds (2.37),

$\hat{\mathcal{F}}_1$ and $\hat{\mathcal{F}}_K$ are in the set G under the CFL condition

$$\Delta t^n \le \lambda \omega_1 \min_{i,\alpha} \left(\Delta x_i^n \Big/ \left(\max \left\{ \left| \frac{p_i^\alpha}{\rho_i^\alpha \sqrt{2e_i^\alpha}} \right|, c_i^\alpha \right\} + |u_i^\alpha| \right) \right) \tag{3.4}$$

with $\lambda = 1/2$ and the sufficient condition

$$\mathbf{U}_i(\hat{x}_i^\alpha) \in G, \ \ \forall \hat{x}_i^\alpha \in S_i, \quad \alpha = 1, ..., K. \tag{3.5}$$

This sufficient condition can be enforced by the linear scaling limiter shown in the next subsection. It is now easy to conclude that $\overline{\mathbf{U}}_i^{n+1} \in G$, since it is a convex combination of elements in G. Thus we can summarize the above results in the following theorem.

Theorem 3.1. *Consider a high order finite volume Lagrangian scheme (2.8) solving the Euler equations (2.1), (2.3) with the general equation of state given by one of (2.5)-(2.7). The numerical flux of the scheme is determined by the HLLC flux described by (2.18)-(2.20) in which the acoustic wavespeeds are chosen as (2.37). If the reconstruction polynomial $\boldsymbol{U}_i(x)$ from the cell average variables $\overline{\boldsymbol{U}}_i^n$ satisfies (3.5), then the scheme (2.8) is positivity-preserving, namely, $\overline{\boldsymbol{U}}_i^{n+1} \in G$ under the time step restriction (3.4) with $\lambda = 1/2$.*

In this paper, we take the three-point Simpson quadrature rule to get the scheme (2.8) up to third order accuracy in the spatial discretization, i.e. $S_i = \{x_{i-\frac{1}{2}}, x_i, x_{i+\frac{1}{2}}\}$, $\omega_1 = \omega_3 = \frac{1}{6}$, $\omega_2 = \frac{2}{3}$.

3.2 The positivity-preserving limiter for high order Lagrangian schemes in the one-dimensional space

At the time level n, assume the reconstruction polynomial in the cell I_i is $\mathbf{U}_i(x) = (\rho_i(x), m_i(x), E_i(x))^T$ with degree k, and the cell average of $\mathbf{U}_i(x)$ is $\overline{\mathbf{U}}_i^n = (\overline{\rho}_i^n, \overline{m}_i^n, \bar{E}_i^n)^T$ which is denoted as $\overline{\mathbf{U}}_i$ in this subsection for simplicity. Under the assumption $\overline{\mathbf{U}}_i \in G \ \forall i$, we would like to modify the reconstruction polynomial $\mathbf{U}_i(x)$ into another polynomial

$$\widetilde{\mathbf{U}}_i(x) = \theta_i(\mathbf{U}_i(x) - \overline{\mathbf{U}}_i) + \overline{\mathbf{U}}_i \tag{3.6}$$

where $\theta_i \in [0, 1]$ is to be determined, such that $\widetilde{\mathbf{U}}_i(x) \in G, \forall x \in S_i$. Following [29, 31], the specific implementation can be taken as follows:

1. First, enforce the positivity of density. Pick a small number ε such that $\overline{\rho}_i \geq \varepsilon$ for all i. In practice, we can choose $\varepsilon = 10^{-13}$. For each cell I_i, compute

$$\widehat{\rho}_i(x) = \theta_i^1 \left[\rho_i(x) - \overline{\rho}_i\right] + \overline{\rho}_i, \quad \theta_i^1 = \min_{x \in S_i} \left\{1, \ \left|\frac{\overline{\rho}_i - \varepsilon}{\overline{\rho}_i - \rho_i(x)}\right|\right\}. \tag{3.7}$$

2. Second, enforce the positivity of the internal energy e for the cells with the ideal EOS or the JWL EOS. Define $\widehat{\mathbf{U}}_i(x) = (\widehat{\rho}_i(x), m_i(x), E_i(x))^T$. For each $x \in S_i$, if $e(\widehat{\mathbf{U}}_i(x)) \geq 0$ set $\theta_x = 1$; otherwise, set

$$\theta_x = \frac{e(\overline{\mathbf{U}}_i)}{e(\overline{\mathbf{U}}_i) - e(\widehat{\mathbf{U}}_i(x))}.$$

For the cells with the stiffened EOS, enforce the positivity of $\tilde{e} = \rho e - p_c$, that is, for each $x \in S_i$, if $\tilde{e}(\widehat{\mathbf{U}}_i(x)) \geq 0$ set $\theta_x = 1$; otherwise, set

$$\theta_x = \frac{\tilde{e}(\overline{\mathbf{U}}_i)}{\tilde{e}(\overline{\mathbf{U}}_i) - \tilde{e}(\widehat{\mathbf{U}}_i(x))}.$$

Then we get the limited polynomial

$$\widetilde{\mathbf{U}}_i(x) = \theta_i^2(\widehat{\mathbf{U}}_i(x) - \overline{\mathbf{U}}_i) + \overline{\mathbf{U}}_i, \quad \theta_i^2 = \min_{x \in S_i} \theta_x. \tag{3.8}$$

It is easy to check that the cell average of $\widetilde{\mathbf{U}}_i(x)$ over I_i is unchanged and is still $\overline{\mathbf{U}}_i^n$, and $\widetilde{\mathbf{U}}_i(\hat{x}_i^\alpha) \in G$ for all α. Moreover, this limiter will not destroy accuracy for smooth solutions, and we refer to [29] for the proof. Thus this positivity-preserving limiter can keep accuracy, conservation and positivity.

3.3 The algorithm for SSP Runge-Kutta time discretization

To improve the accuracy of time discretization for the scheme (2.8), the time marching is implemented by a high order SSP Runge-Kutta type method, for example by the third order SSP Runge-Kutta type method which has the following form in the Lagrangian formulation [5].

Stage 1,

$$x_{i-1/2}^{(1)} = x_{i-1/2}^n + u_{i-1/2}^n \Delta t^n, \qquad \Delta x_i^{(1)} = x_{i+1/2}^{(1)} - x_{i-1/2}^{(1)},$$

$$\overline{\mathbf{U}}_i^{(1)}\Delta x_i^{(1)} = \overline{\mathbf{U}}_i^n \Delta x_i^n + \Delta t^n \mathbf{L}(\overline{\mathbf{U}}_i^n); \tag{3.9}$$

Stage 2,

$$\begin{aligned} &x_{i-1/2}^{(2)} = \frac{3}{4}x_{i-1/2}^n + \frac{1}{4}[x_{i-1/2}^{(1)} + u_{i-1/2}^{(1)}\Delta t^n], \qquad \Delta x_i^{(2)} = x_{i+1/2}^{(2)} - x_{i-1/2}^{(2)}, \\ &\overline{\mathbf{U}}_i^{(2)}\Delta x_i^{(2)} = \frac{3}{4}\overline{\mathbf{U}}_i^n \Delta x_i^n + \frac{1}{4}[\overline{\mathbf{U}}_i^{(1)}\Delta x_i^{(1)} + \Delta t^n \mathbf{L}(\overline{\mathbf{U}}_i^{(1)})]; \end{aligned} \tag{3.10}$$

Stage 3,

$$\begin{aligned} &x_{i-1/2}^{n+1} = \frac{1}{3}x_{i-1/2}^n + \frac{2}{3}[x_{i-1/2}^{(2)} + u_{i-1/2}^{(2)}\Delta t^n], \qquad \Delta x_i^{n+1} = x_{i+1/2}^{n+1} - x_{i-1/2}^{n+1}, \\ &\overline{\mathbf{U}}_i^{n+1}\Delta x_i^{n+1} = \frac{1}{3}\overline{\mathbf{U}}_i^n \Delta x_i^n + \frac{2}{3}[\overline{\mathbf{U}}_i^{(2)}\Delta x_i^{(2)} + \Delta t^n \mathbf{L}(\overline{\mathbf{U}}_i^{(2)})] \end{aligned} \tag{3.11}$$

where $\mathbf{L}$ is the numerical spatial operator representing the right hand of the scheme (2.8).

At each stage, the limiter operation is performed on the conserved variables. Notice that SSP Runge-Kutta schemes are convex combinations of Euler forward time stepping, and are hence conservative, stable and positivity-preserving whenever the Euler forward time stepping is conservative, stable and positivity-preserving.

The algorithm flow chart for the third order positivity-preserving Lagrangian scheme is as follows,

1) Reconstruct the polynomials $\mathbf{U}_i(x)$ at time step n from the cell average $\{\overline{\mathbf{U}}_i^n \in G, i = 1, ..., N\}$ by using the techniques of ENO reconstruction with local characteristic decomposition [5, 6].

2) Perform the positivity-preserving limiter on $\mathbf{U}_i(x)$ to get $\widetilde{\mathbf{U}}_i(x)$ such that $\{\widetilde{\mathbf{U}}_i(x) \in G, \forall x \in S_i\}$.

3) Set $\mathbf{U}_{i-1/2}^+ = \widetilde{\mathbf{U}}_i(x_{i-1/2})$, $\mathbf{U}_{i+1/2}^- = \widetilde{\mathbf{U}}_i(x_{i+1/2})$ and then the numerical flux and the vertex velocity S_* are determined by (2.18)-(2.20).

4) Update the position of each cell vertex and the conserved variables by (3.9) to get $x_{i-1/2}^{(1)}$ and $\overline{\mathbf{U}}_i^{(1)}$.

5) Based on $x_{i-1/2}^{(1)}$ and $\overline{\mathbf{U}}_i^{(1)}$, repeat the above steps 1-3 to get the numerical flux and the vertex velocity for the second stage of the third order SSP Runge-Kutta method.

6) Update the position of each cell vertex and the conserved variables by (3.10) to get $x_{i-1/2}^{(2)}$ and $\overline{\mathbf{U}}_i^{(2)}$.

7) Based on $x_{i-1/2}^{(2)}$ and $\overline{\mathbf{U}}_i^{(2)}$, repeat the above steps 1-3 to get the numerical flux and the vertex velocity for the third stage of the third order SSP Runge-Kutta method.

8) Update the position of each cell vertex and the conserved variables by (3.11) to get x_i^{n+1} and $\overline{\mathbf{U}}_i^{n+1}$.

3.4 High order positivity-preserving Lagrangian scheme in the two-dimensional space

By using a coordinate transformation, we convert the cell $I_{i,j}$ with the general quadrilateral shape in the x-y coordinates to the square $[-\frac{1}{2},\frac{1}{2}]\times[-\frac{1}{2},\frac{1}{2}]$ in the ξ-η coordinates (see Figure 3.1). The inverse of this mapping, namely the mapping from the ξ-η coordinates to the x-y coordinates, is bilinear. Define the set of Gauss-Lobatto quadrature points for the cell $I_{i,j}$ to be $S_{i,j} = \{(x_{\alpha,\beta}, y_{\alpha,\beta}), \alpha = 1, ..., K, \beta = 1, ..., K\}$, which are the pre-images under the coordinate transformation of the Gauss-Lobatto quadrature points in the square $[-\frac{1}{2},\frac{1}{2}]\times[-\frac{1}{2},\frac{1}{2}]$. We require the Gauss-Lobatto quadrature to be exact for polynomials of degree $2k+1$. This is because a polynomial of degree k in the x-y coordinates becomes a polynomial of degree $2k$ in the ξ-η coordinates, and the Jacobian of the coordinate transformation is a linear function. For example, to construct a second order Lagrangian scheme, the 3×3-point tensor product Simpson quadrature rule can be applied where the quadrature points consist of the cell vertices, the middle points of the cell edges and the cell center. $\omega_1 = \omega_3 = \frac{1}{6}, \omega_2 = \frac{2}{3}$ (see Figure 3.1). Then we can decompose the cell average $\overline{\mathbf{U}}_{i,j}^n$ as follows,

$$\overline{\mathbf{U}}_{i,j}^n = \frac{1}{A_{i,j}^n}\iint_{I_{i,j}} \mathbf{U}_{i,j}(x,y)dxdy$$

$$
\begin{aligned}
&= \frac{1}{A_{i,j}^n}\int_{-\frac{1}{2}}^{\frac{1}{2}}\int_{-\frac{1}{2}}^{\frac{1}{2}} \mathbf{U}_{i,j}(\mathbf{g}_{i,j}(\xi,\eta))\left|\frac{\partial \mathbf{g}_{i,j}(\xi,\eta)}{\partial(\xi,\eta)}\right| d\xi d\eta \\
&= \frac{1}{A_{i,j}^n}\sum_{\alpha=1}^{K}\sum_{\beta=1}^{K}\omega_\alpha\omega_\beta \mathbf{U}_{i,j}(\mathbf{g}_{i,j}(\xi_\alpha,\eta_\beta))\left|\frac{\partial \mathbf{g}_{i,j}(\xi,\eta)}{\partial(\xi,\eta)}\right|_{(\xi_\alpha,\eta_\beta)} \\
&= \frac{1}{A_{i,j}^n}\sum_{\alpha=1}^{K}\sum_{\beta=1}^{K}\omega_\alpha\omega_\beta \left|\frac{\partial \mathbf{g}_{i,j}(\xi,\eta)}{\partial(\xi,\eta)}\right|_{(\xi_\alpha,\eta_\beta)} \mathbf{U}_{i,j}^{\alpha,\beta}
\end{aligned}
$$

where $\{\mathbf{U}_{i,j}^{\alpha,\beta}, \alpha,\beta = 1,...,K\}$ are the values of $\mathbf{U}_{i,j}(x,y)$ at the corresponding Gauss-Lobatto quadrature points. $|\frac{\partial \mathbf{g}_{i,j}(\xi,\eta)}{\partial(\xi,\eta)}|$ is the Jacobian for the coordinate transformation. Specifically,

$$
\mathbf{g}_{i,j}(\xi,\eta) == \begin{pmatrix} a_1\xi\eta + a_2\xi + a_3\eta + a_4 \\ b_1\xi\eta + b_2\xi + b_3\eta + b_4 \end{pmatrix}
$$

$$
|\frac{\partial \mathbf{g}_{i,j}(\xi,\eta)}{\partial(\xi,\eta)}|_{(\xi_\alpha,\eta_\beta)} = (a_2b_1 - a_1b_2)\xi_\alpha + (a_1b_3 - a_3b_1)\eta_\beta + (a_2b_3 - a_3b_2)
$$

where

$$
\begin{aligned}
a_1 &= x_{i-\frac{1}{2},j-\frac{1}{2}} + x_{i+\frac{1}{2},j+\frac{1}{2}} - x_{i+\frac{1}{2},j-\frac{1}{2}} - x_{i-\frac{1}{2},j+\frac{1}{2}}, \\
a_2 &= \frac{1}{2}(x_{i+\frac{1}{2},j-\frac{1}{2}} + x_{i+\frac{1}{2},j+\frac{1}{2}} - x_{i-\frac{1}{2},j-\frac{1}{2}} - x_{i-\frac{1}{2},j+\frac{1}{2}}), \\
a_3 &= \frac{1}{2}(x_{i+\frac{1}{2},j+\frac{1}{2}} + x_{i-\frac{1}{2},j+\frac{1}{2}} - x_{i-\frac{1}{2},j-\frac{1}{2}} - x_{i+\frac{1}{2},j-\frac{1}{2}}), \\
a_4 &= \frac{1}{4}(x_{i-\frac{1}{2},j-\frac{1}{2}} + x_{i+\frac{1}{2},j-\frac{1}{2}} + x_{i+\frac{1}{2},j+\frac{1}{2}} + x_{i-\frac{1}{2},j+\frac{1}{2}}), \\
b_1 &= y_{i-\frac{1}{2},j-\frac{1}{2}} + y_{i+\frac{1}{2},j+\frac{1}{2}} - y_{i+\frac{1}{2},j-\frac{1}{2}} - y_{i-\frac{1}{2},j+\frac{1}{2}}, \\
b_2 &= \frac{1}{2}(y_{i+\frac{1}{2},j-\frac{1}{2}} + y_{i+\frac{1}{2},j+\frac{1}{2}} - y_{i-\frac{1}{2},j-\frac{1}{2}} - y_{i-\frac{1}{2},j+\frac{1}{2}}), \\
b_3 &= \frac{1}{2}(y_{i+\frac{1}{2},j+\frac{1}{2}} + y_{i-\frac{1}{2},j+\frac{1}{2}} - y_{i-\frac{1}{2},j-\frac{1}{2}} - y_{i+\frac{1}{2},j-\frac{1}{2}}) \\
b_4 &= \frac{1}{4}(y_{i-\frac{1}{2},j-\frac{1}{2}} + y_{i+\frac{1}{2},j-\frac{1}{2}} + y_{i+\frac{1}{2},j+\frac{1}{2}} + y_{i-\frac{1}{2},j+\frac{1}{2}}).
\end{aligned}
$$

Denote $|J|_{i,j}^{\alpha,\beta} = |\frac{\partial \mathbf{g}_{i,j}(\xi,\eta)}{\partial(\xi,\eta)}|_{(\xi_\alpha,\eta_\beta)}$, $\tilde{\omega}_{\alpha,\beta} = \omega_\alpha\omega_\beta|J|_{i,j}^{\alpha,\beta}$, then we have

$$
\begin{aligned}
&\bar{\mathbf{U}}_{i,j}^n = \frac{1}{2}\overline{\mathbf{U}}_{i,j}^n + \frac{1}{2}\overline{\mathbf{U}}_{i,j}^n \qquad (3.12) \\
&= \frac{1}{2A_{i,j}^n}\left[\sum_{\alpha=1}^{K}\omega_1\omega_\alpha|J|_{i,j}^{1,\alpha}\mathbf{U}_{1,\alpha}^{int(I_{i,j})} + \sum_{\alpha=1}^{K}\omega_K\omega_\alpha|J|_{i,j}^{K,\alpha}\mathbf{U}_{3,\alpha}^{int(I_{i,j})} + \sum_{\beta=2}^{K-1}\sum_{\alpha=1}^{K}\tilde{\omega}_{\beta,\alpha}\mathbf{U}_{i,j}^{\beta,\alpha}\right]
\end{aligned}
$$

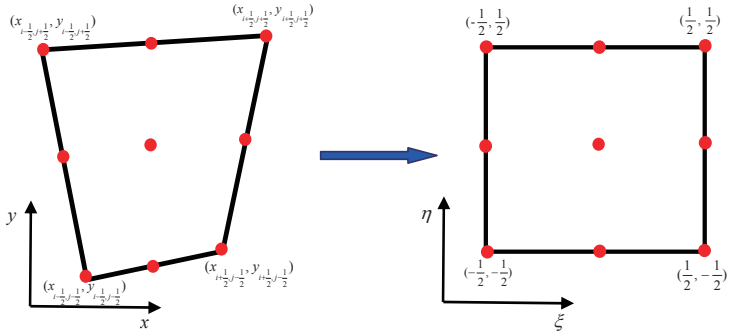

Figure 3.1: Transformation from x-y coordinates to ξ-η coordinates for the calculation of integration.

$$+\frac{1}{2A_{i,j}^n}\left[\sum_{\alpha=1}^{K}\omega_\alpha\omega_1|J|_{i,j}^{\alpha,1}\mathbf{U}_{2,\alpha}^{int(I_{i,j})}+\sum_{\alpha=1}^{K}\omega_\alpha\omega_K|J|_{i,j}^{\alpha,K}\mathbf{U}_{4,\alpha}^{int(I_{i,j})}+\sum_{\beta=2}^{K-1}\sum_{\alpha=1}^{K}\tilde{\omega}_{\alpha,\beta}\mathbf{U}_{i,j}^{\alpha,\beta}\right]$$

where $\{\mathbf{U}_{m,\alpha}^{int(I_{i,j})}, m=1,...,4\}$ are the values of the reconstruction polynomial $\mathbf{U}_{i,j}(x,y)$ for the cell $I_{i,j}$ at the Gauss-Lobatto quadrature points along its left, bottom, right and top cell boundaries respectively. Specifically we have $\mathbf{U}_{1,\alpha}^{int(I_{i,j})}=\mathbf{U}_{i,j}^{1,\alpha}$, $\mathbf{U}_{3,\alpha}^{int(I_{i,j})}=\mathbf{U}_{i,j}^{K,\alpha}$ and $\mathbf{U}_{2,\alpha}^{int(I_{i,j})}=\mathbf{U}_{i,j}^{\alpha,1}$, $\mathbf{U}_{4,\alpha}^{int(I_{i,j})}=\mathbf{U}_{i,j}^{\alpha,K}$.

Substituting (2.42) into the scheme (2.40), we get the general form of high order Lagrangian schemes in two-dimensional space with forward Euler time discretization,

$$\overline{\mathbf{U}}_{i,j}^{n+1}A_{i,j}^{n+1}-\overline{\mathbf{U}}_{i,j}^{n}A_{i,j}^{n}=-\Delta t\sum_{m=1}^{4}\sum_{\alpha=1}^{K}\omega_\alpha\hat{\mathbf{F}}(\mathbf{U}_{m,\alpha}^{int(I_{i,j})},\mathbf{U}_{m,\alpha}^{ext(I_{i,j})},\mathbf{n}_{I_{i,j}}^{m})l_{i,j}^{m}. \tag{3.13}$$

The numerical flux $\hat{\mathbf{F}}$ along the cell edge is determined by the formulas (2.43)-(2.44).

We choose the same Gauss-Lobatto quadrature points for the line integral of the numerical flux as those used in (3.12) along each cell edge. Substituting (3.12) into the scheme (3.13) and noticing $\omega_1=\omega_K$, then we get

$$\begin{aligned}\overline{\mathbf{U}}_{i,j}^{n+1}A_{i,j}^{n+1}=&\frac{1}{2}\left[\sum_{\beta=2}^{K-1}\sum_{\alpha=1}^{K}\tilde{\omega}_{\beta,\alpha}\mathbf{U}_{i,j}^{\beta,\alpha}+\sum_{\beta=2}^{K-1}\sum_{\alpha=1}^{K}\tilde{\omega}_{\alpha,\beta}\mathbf{U}_{i,j}^{\alpha,\beta}\right]\\&+\frac{1}{2}\omega_1\sum_{\alpha=1}^{K}\omega_\alpha\left[\mathbf{U}_{1,\alpha}^{int(I_{i,j})}|J|_{i,j}^{1,\alpha}+\mathbf{U}_{2,\alpha}^{int(I_{i,j})}|J|_{i,j}^{\alpha,1}+\mathbf{U}_{3,\alpha}^{int(I_{i,j})}|J|_{i,j}^{K,\alpha}+\mathbf{U}_{4,\alpha}^{int(I_{i,j})}|J|_{i,j}^{\alpha,K}\right]\\&-\Delta t\sum_{m=1}^{4}\sum_{\alpha=1}^{K}\omega_\alpha\hat{\mathbf{F}}(\mathbf{U}_{m,\alpha}^{int(I_{i,j})},\mathbf{U}_{m,\alpha}^{ext(I_{i,j})},\mathbf{n}_{I_{i,j}}^{m})l_{i,j}^{m}.\end{aligned}$$

By adding and subtracting $\Delta t\hat{\mathbf{F}}(\mathbf{U}_{1,\alpha}^{int(I_{i,j})}, \mathbf{U}_{m,\alpha}^{int(I_{i,j})}, \mathbf{n}_{I_{i,j}}^{m})l_{i,j}^{m}, m = 2, ..., 4$, we then get

$$\begin{aligned}\overline{\mathbf{U}}_{i,j}^{n+1} A_{i,j}^{n+1} = & \quad \frac{1}{2}\left[\sum_{\beta=2}^{K-1}\sum_{\alpha=1}^{K}\tilde{\omega}_{\beta,\alpha}\mathbf{U}_{i,j}^{\beta,\alpha} + \sum_{\beta=2}^{K-1}\sum_{\alpha=1}^{K}\tilde{\omega}_{\alpha,\beta}\mathbf{U}_{i,j}^{\alpha,\beta}\right] \\ & + \quad \frac{\omega_1}{2}\sum_{\alpha=1}^{K}\omega_\alpha[\hat{\mathcal{F}}_\alpha^1 + \hat{\mathcal{F}}_\alpha^2 + \hat{\mathcal{F}}_\alpha^3 + \hat{\mathcal{F}}_\alpha^4] \end{aligned} \tag{3.14}$$

where

$$\begin{aligned}
\hat{\mathcal{F}}_\alpha^1 &= \mathbf{U}_{1,\alpha}^{int(I_{i,j})}|J|_{i,j}^{1,\alpha} - \frac{2\Delta t}{\omega_1}\Big[\hat{\mathbf{F}}(\mathbf{U}_{1,\alpha}^{int(I_{i,j})}, \mathbf{U}_{1,\alpha}^{ext(I_{i,j})}, \mathbf{n}_{I_{i,j}}^{1})l_{i,j}^{1} + \hat{\mathbf{F}}(\mathbf{U}_{1,\alpha}^{int(I_{i,j})}, \mathbf{U}_{2,\alpha}^{int(I_{i,j})}, \mathbf{n}_{I_{i,j}}^{2})l_{i,j}^{2} \\
&\qquad + \hat{\mathbf{F}}(\mathbf{U}_{1,\alpha}^{int(I_{i,j})}, \mathbf{U}_{3,\alpha}^{int(I_{i,j})}, \mathbf{n}_{I_{i,j}}^{3})l_{i,j}^{3} + \hat{\mathbf{F}}(\mathbf{U}_{1,\alpha}^{int(I_{i,j})}, \mathbf{U}_{4,\alpha}^{int(I_{i,j})}, \mathbf{n}_{I_{i,j}}^{4})l_{i,j}^{4}\Big], \\
\hat{\mathcal{F}}_\alpha^2 &= \mathbf{U}_{2,\alpha}^{int(I_{i,j})}|J|_{i,j}^{\alpha,1} - \frac{2l_{i,j}^2\Delta t}{\omega_1}[\hat{\mathbf{F}}(\mathbf{U}_{2,\alpha}^{int(I_{i,j})}, \mathbf{U}_{2,\alpha}^{ext(I_{i,j})}, \mathbf{n}_{I_{i,j}}^{2}) - \hat{\mathbf{F}}(\mathbf{U}_{1,\alpha}^{int(I_{i,j})}, \mathbf{U}_{2,\alpha}^{int(I_{i,j})}, \mathbf{n}_{I_{i,j}}^{2})], \\
\hat{\mathcal{F}}_\alpha^3 &= \mathbf{U}_{3,\alpha}^{int(I_{i,j})}|J|_{i,j}^{K,\alpha} - \frac{2l_{i,j}^3\Delta t}{\omega_1}[\hat{\mathbf{F}}(\mathbf{U}_{3,\alpha}^{int(I_{i,j})}, \mathbf{U}_{3,\alpha}^{ext(I_{i,j})}, \mathbf{n}_{I_{i,j}}^{3}) - \hat{\mathbf{F}}(\mathbf{U}_{1,\alpha}^{int(I_{i,j})}, \mathbf{U}_{3,\alpha}^{int(I_{i,j})}, \mathbf{n}_{I_{i,j}}^{3})], \\
\hat{\mathcal{F}}_\alpha^4 &= \mathbf{U}_{4,\alpha}^{int(I_{i,j})}|J|_{i,j}^{\alpha,K} - \frac{2l_{i,j}^4\Delta t}{\omega_1}[\hat{\mathbf{F}}(\mathbf{U}_{4,\alpha}^{int(I_{i,j})}, \mathbf{U}_{4,\alpha}^{ext(I_{i,j})}, \mathbf{n}_{I_{i,j}}^{4}) - \hat{\mathbf{F}}(\mathbf{U}_{1,\alpha}^{int(I_{i,j})}, \mathbf{U}_{4,\alpha}^{int(I_{i,j})}, \mathbf{n}_{I_{i,j}}^{4})].
\end{aligned}$$

Under the time step restriction,

$$\Delta t^n \le \frac{\omega_1}{2}\lambda \min_{i,j,\alpha,\beta}\left\{\frac{|J|_{i,j}}{\sum_{m=1,4} l_{i,j}^m} \Big/ \left(\max\left\{\left|\frac{p_{i,j}^{\alpha,\beta}}{\rho_{i,j}^{\alpha,\beta}\sqrt{2e_{i,j}^{\alpha,\beta}}}\right|, c_{i,j}^{\alpha,\beta}\right\} + |\mathbf{u}_{i,j}^{\alpha,\beta}|\right)\right\} \tag{3.15}$$

where $|J|_{i,j} = \min_{\alpha=1,K}\{|J|_{i,j}^{\alpha,1}, |J|_{i,j}^{\alpha,K}, |J|_{i,j}^{1,\alpha}, |J|_{i,j}^{K,\alpha}\}$, $\hat{\mathcal{F}}^1$ is a formal two-dimensional first order positivity-preserving scheme, namely, the same type as (2.45), therefore $\hat{\mathcal{F}}_\alpha^1 \in G$. $\hat{\mathcal{F}}^2$, $\hat{\mathcal{F}}^3$ and $\hat{\mathcal{F}}^4$ are formal one-dimensional first order positivity-preserving schemes (like the scheme (2.10)), thus $\hat{\mathcal{F}}^2, \hat{\mathcal{F}}^3, \hat{\mathcal{F}}^4 \in G$. Notice that $\overline{\mathbf{U}}^{n+1}$ is a convex combination of $\mathbf{U}^{\alpha,\beta}$ and $\hat{\mathcal{F}}_\alpha^m$. Since G is a convex set, we have $\overline{\mathbf{U}}^{n+1} \in G$ if $\mathbf{U}^{\alpha,\beta} \in G$. We have therefore the following theorem.

Theorem 3.2. *Consider a finite volume Lagrangian scheme (3.13) with the HLLC flux (2.43)-(2.44) solving the Euler equations (2.1), (2.3) with the general equation of state given by one of (2.5)-(2.7). If the reconstruction polynomial for the cell average variables $\overline{\boldsymbol{U}}_{i,j}^n$ satisfies $\boldsymbol{U}_{i,j}^{\alpha,\beta} \in G$, $\forall \alpha, \beta = 1, ..., K, i = 1, ..., M, j = 1, ..., N$, then the scheme (3.13) is positivity-preserving, namely, $\overline{\boldsymbol{U}}_{i,j}^{n+1} \in G$ under the time step restriction (3.15) with $\lambda = 1/2$.*

Remark 3.1. *Notice that the time step restriction (3.15) would give a positive time step only if* $\{|J|_{i,j}^{\alpha,\beta} > 0, \alpha, \beta = 1, .., K\}$. *That is, we can guarantee positivity-preserving only if the shape of all the cells keeps convex.*

Remark 3.2. *In this paper, as the reconstruction polynomial to determine* $\mathbf{U}^{int}, \mathbf{U}^{ext}$ *are obtained by the high order ENO reconstruction with Roe-type characteristic decomposition along each cell edge, they will have multiple values at the vertices which are the joint Gauss-Lobatto quadrature points of all their connecting edges. That is why we should split* $\overline{\boldsymbol{U}}_{i,j}^{n}$ *into two parts like (3.12).*

Similar SSP Runge-Kutta method introduced in the subsection 3.3 can also be used on the scheme (3.13) to get high order accuracy in time discretization, which can keep the positivity-preserving property due to its convexity.

3.5 The positivity-preserving limiter for the high order Lagrangian scheme in the two-dimensional space

At the time level n, we will perform the limiter on the two series of polynomials belonging to $\{\mathbf{U}_{1,\alpha}^{int(I_{i,j})}, \mathbf{U}_{3,\alpha}^{int(I_{i,j})}, \mathbf{U}_{i,j}^{\beta,\alpha}, \alpha = 1, ..., K, \beta = 2, ..., K-1\}$ and $\{\mathbf{U}_{2,\alpha}^{int(I_{i,j})}, \mathbf{U}_{4,\alpha}^{int(I_{i,j})}, \mathbf{U}_{i,j}^{\alpha,\beta}, \alpha = 1, ..., K, \beta = 2, ..., K-1\}$ sequentially and then get the modified values of $\{\widetilde{\mathbf{U}}_{m,\alpha}^{int(I_{i,j})}, \alpha = 1, ..., K, m = 1, ..., 4\}$ which are used in the scheme (3.13). The implementation taken on these two series of polynomials is similar to that for the high order scheme in the one-dimensional space which can be described as follows.

Assuming a reconstruction polynomial in the cell $I_{i,j}$ is $\mathbf{U}_{i,j}(x,y) = (\rho_{i,j}(x,y), \mathbf{m}_{i,j}(x,y), E_{i,j}(x,y))^T$ with degree k, and the cell average of $\mathbf{U}_{i,j}(x,y)$ is $\overline{\mathbf{U}}_{i,j} = (\overline{\rho}_{i,j}, \overline{\mathbf{m}}_{i,j}, \overline{E}_{i,j})^T$, we next modify it into another polynomial

$$\widetilde{\mathbf{U}}_{i,j}(x,y) = \theta_{i,j}(\mathbf{U}_{i,j}(x,y) - \overline{\mathbf{U}}_{i,j}) + \overline{\mathbf{U}}_{i,j} \tag{3.16}$$

where $\theta_{i,j} \in [0,1]$ is to be determined, such that $\widetilde{\mathbf{U}}_{i,j}(x,y) \in G, \forall (x,y) \in S_{i,j}$.

1. First, enforce the positivity of density. Pick a small number ε such that $\overline{\rho}_{i,j} \geq \varepsilon$ for all i, j. In practice, we can choose $\varepsilon = 10^{-13}$. For each element $I_{i,j}$, compute

$$\widehat{\rho}_{i,j}(x,y) = \theta^1_{i,j}\left[\rho_{i,j}(x,y) - \overline{\rho}_{i,j}\right] + \overline{\rho}_{i,j}, \quad \theta^1_{i,j} = \min_{(x,y)\in S_{i,j}} \left\{1, \left|\frac{\overline{\rho}_{i,j} - \varepsilon}{\overline{\rho}_{i,j} - \rho_{i,j}(x,y)}\right|\right\}. \tag{3.17}$$

2. Second, enforce the positivity of internal energy e for the cells with the ideal EOS or the JWL EOS. Define $\widehat{\mathbf{U}}_{i,j}(x,y) = (\widehat{\rho}_{i,j}(x,y), \mathbf{m}_{i,j}(x,y), E_{i,j}(x,y))^T$. For each $(x,y) \in S_{i,j}$, if $e(\widehat{\mathbf{U}}_{i,j}(x,y)) \geq 0$ set $\theta_{x,y} = 1$; otherwise, set

$$\theta_{x,y} = \frac{e(\overline{\mathbf{U}}_{i,j})}{e(\overline{\mathbf{U}}_{i,j}) - e(\widehat{\mathbf{U}}_{i,j}(x,y))}. \tag{3.18}$$

   Similarly, for the cells with the stiffened EOS, enforce the positivity of $\tilde{e} = \rho e - p_c$, that is, for each $(x,y) \in S_{i,j}$, if $\tilde{e}(\widehat{\mathbf{U}}_{i,j}(x,y)) \geq 0$ set $\theta_{x,y} = 1$; otherwise, set

$$\theta_{x,y} = \frac{\tilde{e}(\overline{\mathbf{U}}_{i,j})}{\tilde{e}(\overline{\mathbf{U}}_{i,j}) - \tilde{e}(\widehat{\mathbf{U}}_{i,j}(x,y))}. \tag{3.19}$$

   Then the final limited polynomial is obtained as follows,

$$\widetilde{\mathbf{U}}_{i,j}(x,y) = \theta^2_{i,j}(\widehat{\mathbf{U}}_{i,j}(x,y) - \overline{\mathbf{U}}_{i,j}) + \overline{\mathbf{U}}_{i,j}, \quad \theta^2_{i,j} = \min_{(x,y)\in S_{i,j}} \theta_{x,y}. \tag{3.20}$$

The preservation of conservation, positivity and accuracy of the polynomials $\widetilde{\mathbf{U}}_{i,j}(x,y)$ can be proven as in the one-dimensional case, see [29] for more details.

The flow chart for the second order positivity-preserving Lagrangian scheme in the two-dimensional space is similar to that in subsection 3.3 for the one-dimensional high order positivity-preserving Lagrangian scheme.

Remark 3.3. *In practice, we do not need to limit each internal Gauss-Lobatto quadrature point $\boldsymbol{U}^{\alpha,\beta}_{i,j}$. As discussed in [31], due to the mean value theorem, there exist points $(x^*, y^*) \in I_{i,j}$ and $(x^{**}, y^{**}) \in I_{i,j}$ such that*

$$\rho_{i,j}(x^*, y^*) \;=\; \frac{1}{\sum_{\beta=2}^{K-1}\sum_{\alpha=1}^{K}\tilde{\omega}_{\beta,\alpha}} \sum_{\beta=2}^{K-1}\sum_{\alpha=1}^{K}\tilde{\omega}_{\beta,\alpha}\rho^{\beta,\alpha}_{i,j}$$

$$= \frac{1}{\sum_{\beta=2}^{K-1}\sum_{\alpha=1}^{K}\tilde{\omega}_{\beta,\alpha}}(\overline{\rho}_{i,j} - \sum_{\alpha=1}^{K}\omega_1\omega_\alpha|J|_{i,j}^{1,\alpha}\rho_{1,\alpha}^{int(I_{i,j})} - \sum_{\alpha=1}^{K}\omega_K\omega_\alpha|J|_{i,j}^{K,\alpha}\rho_{3,\alpha}^{int(I_{i,j})}),$$

$$\rho_{i,j}(x^{**},y^{**}) = \frac{1}{\sum_{\beta=2}^{K-1}\sum_{\alpha=1}^{K}\tilde{\omega}_{\alpha,\beta}}\sum_{\beta=2}^{K-1}\sum_{\alpha=1}^{K}\tilde{\omega}_{\alpha,\beta}\rho_{i,j}^{\alpha,\beta}$$

$$= \frac{1}{\sum_{\beta=2}^{K-1}\sum_{\alpha=1}^{K}\tilde{\omega}_{\alpha,\beta}}(\overline{\rho}_{i,j} - \sum_{\alpha=1}^{K}\omega_\alpha\omega_1|J|_{i,j}^{\alpha,1}\rho_{2,\alpha}^{int(I_{i,j})} - \sum_{\alpha=1}^{K}\omega_\alpha\omega_K|J|_{i,j}^{\alpha,K}\rho_{4,\alpha}^{int(I_{i,j})}).$$

Thus to guarantee all the terms at the right hand side of (3.14) to be density positive, in the implementation, only $\rho_{i,j}(x^*,y^*), \rho_{i,j}(x^{**},y^{**})$ *and* $\{\rho_{m,\alpha}^{int(I_{i,j})}, \alpha = 1,...,K, m = 1,...,4\}$ *need to be involved to determine* $\theta_{i,j}^1$*. Similar simplified operations can be done for* e *and* $\tilde{e}$*.*

Remark 3.4. *In practice, we do not need to know explicitly the polynomials* $\mathbf{U}_{i,j}(x,y)$ *and* $\widetilde{\mathbf{U}}_{i,j}(x,y)$ *either.* θ *defined by (3.17)-(3.19) can be calculated without the explicit expression of the approximation polynomial* $\mathbf{U}_{i,j}(x,y)$ *or the locations* $(x^*,y^*),(x^{**},y^{**})$*. We only need to know the existence of such polynomials to prove the accuracy of the limiter. Instead only the values of* $\mathbf{U}_{m,\alpha}^{int(I_{i,j})}, \mathbf{U}_{m,\alpha}^{ext(I_{i,j})}$ *at the Gauss-Lobatto quadrature points along the cell edges should be modified by (3.20) which will be used to construct the scheme. Thus the implementation for the above procedures becomes very simple.*

4 Numerical tests

In this section, we choose several challenging numerical examples in one- and two-dimensional spaces to demonstrate the performance of our first order and high order positivity-preserving Lagrangian schemes. The examples involve the ideal and non-ideal multi-material problems. All these examples encounter the problem of negative internal energy or negative c^2 if the usual high order Lagrangian scheme without the positivity-preserving limiter is applied. $\lambda = 0.5$ is applied in these simulations.

4.1 One-dimensional tests

Example 4.1. *Numerical convergence study.*

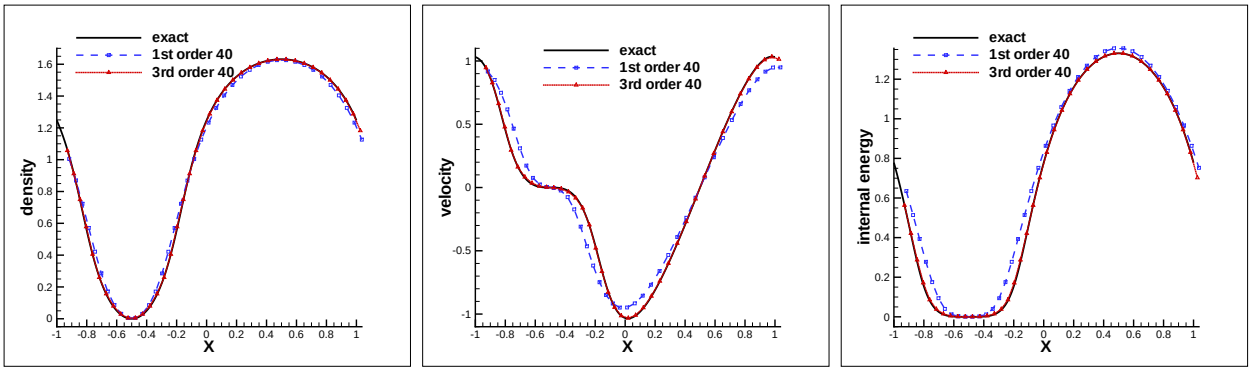

Figure 4.1: The results of the one-dimensional smooth isentropic problem at $t = 0.1$. Left: density; Middle: velocity; Right: internal energy.

We first test the accuracy of our schemes on a isentropic problem with smooth solutions. Its initial condition is:

$$\rho(x,0) = 1 + 0.9999995\sin(\pi x), \qquad u(x,0) = 0, \qquad p(x,0) = \rho^{\gamma}(x,0), \qquad x \in [-1,1]$$

with $\gamma = 3$ and the periodic boundary condition. For this kind of special isentropic problem, the Euler equations are equivalent to the two Burgers equations in terms of their two Riemann invariants for which an analytical solution is easy to obtain. Figure 4.1 shows the computed results at $t = 0.1$ for the first order Lagrangian scheme and third order Lagrangian scheme with the positivity-preserving limiter using 40 initially uniform cells. In Tables 4.1-4.2, we summarize the errors and numerical rate of convergence of our first and third order Lagrangian schemes at $t = 0.1$. The percentage of the cells in which the positivity-preserving limiter has been performed is also listed in Table 4.2. We can clearly see from Tables 4.1 and 4.2 that the first order Lagrangian scheme and third order Lagrangian scheme with the positivity-preserving limiter achieve the designed order of accuracy both in the L_1 and L_∞ norms.

Example 4.2. *Interaction of blast waves.*

The problem of interaction of blast waves is a typical low internal energy problem involv-

Table 4.1: Errors of the first order Lagrangian scheme on 1D meshes using N_x initially uniform cells.

N_x	Norm	Density	order	Momentum	order	Energy	order
100	L_1	0.94E-2		0.29E-1		0.26E-1	
	L_∞	0.22E-1		0.65E-1		0.72E-1	
200	L_1	0.48E-2	0.97	0.15E-1	0.96	0.14E-1	0.95
	L_∞	0.11E-1	0.95	0.33E-1	0.96	0.38E-1	0.93
400	L_1	0.24E-2	0.98	0.76E-2	0.98	0.69E-2	0.98
	L_∞	0.58E-2	0.98	0.17E-1	0.98	0.19E-1	0.96
800	L_1	0.12E-2	0.99	0.38E-2	0.99	0.35E-2	0.99
	L_∞	0.29E-2	0.99	0.86E-2	0.99	0.99E-2	0.98

Table 4.2: Errors of the third order ENO Lagrangian scheme with the positivity-preserving limiter on 1D meshes using N_x initially uniform cells.

N_x	Norm	Density	order	Momentum	order	Energy	order	limited cells
100	L_1	0.11E-3		0.14E-3		0.14E-3		2%
	L_∞	0.85E-3		0.67E-3		0.60E-3		
200	L_1	0.14E-4	2.94	0.17E-4	3.07	0.18E-4	2.96	1%
	L_∞	0.85E-4	3.32	0.85E-4	2.98	0.78E-4	2.95	
400	L_1	0.16E-5	3.07	0.21E-5	3.00	0.23E-5	2.99	0.5%
	L_∞	0.11E-4	2.92	0.11E-4	3.00	0.98E-5	2.98	
800	L_1	0.20E-6	3.04	0.27E-6	3.00	0.28E-6	3.00	0.25%
	L_∞	0.11E-5	3.36	0.13E-5	3.00	0.12E-5	2.99	

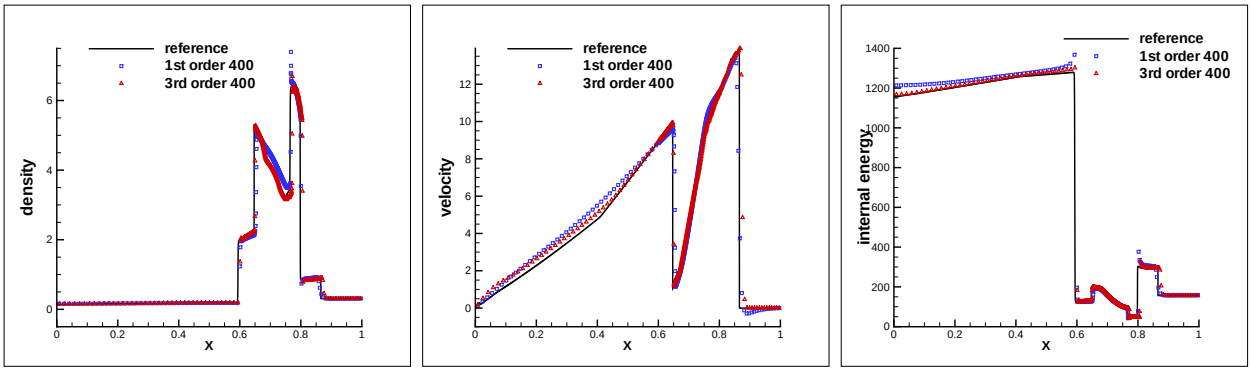

Figure 4.2: The results of the blast wave problem at $t = 0.038$. Left: density; Middle: velocity; Right: internal energy.

ing shocks. The initial data are

$$\rho = 1, \qquad u = 1, \qquad p = \begin{cases} 10^3, & 0 < x < 0.1 \\ 10^{-2}, & 0.1 < x < 0.9 \\ 10^2, & 0.9 < x < 1.0. \end{cases}$$

The working fluid is described by an perfect gas with $\gamma = 1.4$. The reflective boundary condition is applied at both $x = 0$ and $x = 1$. In Figure 4.2, the computed density, velocity and internal energy with 400 initially uniform cells at the final time $t = 0.038$ are plotted against the reference "exact" solution, which is computed using a fifth order Eulerian WENO scheme [15] with 16000 grid points. We can see that both density and internal energy can keep positive in this problem for our first and third order Lagrangian schemes, and the higher order scheme has a better resolution than the first order scheme. Meanwhile, we also notice that some overshoots appear near the discontinuity such as the contact wave, in these figures and in some examples later. Such overshoots are caused by the Lagrangian framework rather than by the high order ENO reconstruction, since they are already present for the first order scheme which does not involve any ENO reconstruction.

Example 4.3. *The Leblanc shock tube problem.*

In this extreme shock tube problem, the computational domain is $[0, 9]$ filled with a perfect gas with $\gamma = 5/3$. The initial condition consists of large ratio jumps for the energy

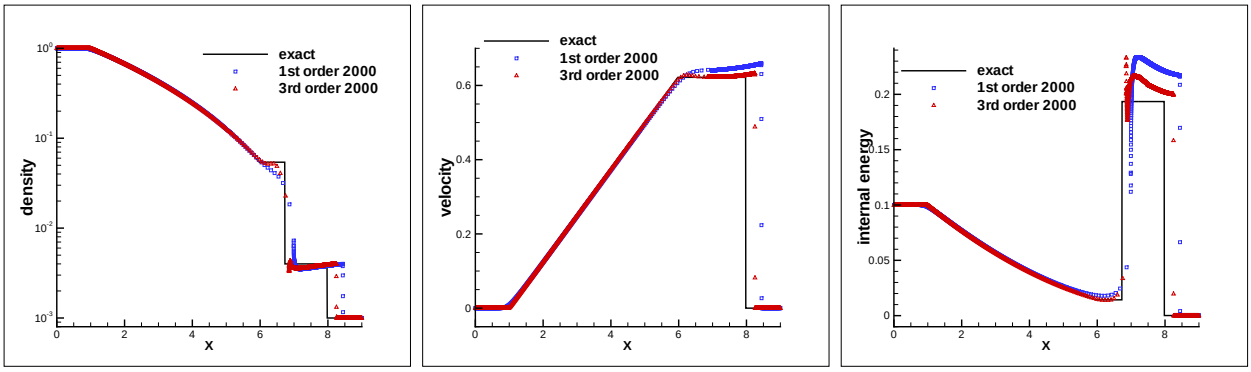

Figure 4.3: The results of the Leblanc problem at $t = 6.0$. Left: density; Middle: velocity; Right: internal energy.

and density and is given by the following data

$$(\rho, u, e) = \begin{cases} (1, \quad 0, \quad 0.1), & 0 \le x < 3 \\ (0.001, 0, 10^{-7}), & 3 < x \le 9. \end{cases}$$

It is very difficult for a scheme to obtain accurate positions of the contact and shock discontinuities in such a severe test case [27]. The results of density, velocity and internal energy for our first order and third order Lagrangian schemes with the HLLC flux and the positivity-preserving limiter are shown in Figure 4.3 with 2000 initially uniform cells at $t = 6$. By comparing with the exact solution, we can observe that the property of positivity is well preserved and the shape and position of the contact discontinuity and the shock can be maintained better when the higher order scheme is used. The high order Lagrangian scheme without the positivity-preserving limiter will blow up for this example.

Example 4.4. *The 123 problem.*

We consider a one-dimensional low density and low pressure problem for perfect gas. The initial condition is

$$(\rho, u, p, \gamma) = \begin{cases} (1, -2, 0.4, 1.4), & -4 \le x \le 0 \\ (1, \quad 2, 0.4, 1.4), & 0 < x \le 4. \end{cases}$$

The exact solution contains vacuum. The results of our first and third order positivity-preserving Lagrangian schemes with 400 initially uniform cells compared with the exact

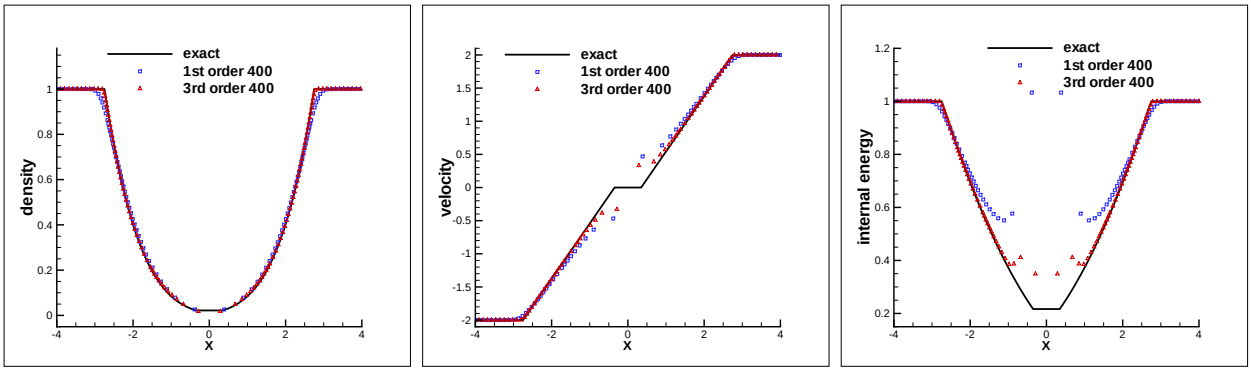

Figure 4.4: The results of the 123 problem with 400 cells at $t = 1.0$. Left: density; Middle: velocity; Right: internal energy.

solution at $t = 1.0$ are shown in Figure 4.4. We can see that the low internal energy and the low density are both captured correctly with the higher resolution for the higher order scheme. Without the positivity-preserving limiter, the high order Lagrangian scheme will blow up for this example. In these figures, we also observe that the resolution for the velocity and internal energy near the origin (vacuum) in the Lagrangian simulation is less satisfactory as that in the Eulerian simulation. A possible reason for this phenomena is that much fewer grid points are located in this region in the Lagrangian simulation as the fluid moves outward in both directions.

Example 4.5. *The gas-liquid shock-tube problem [24].*

This severe water-air shock tube problem has a density ratio of 200. This shock tube problem is considered to illustrate the performance of the schemes for multi-material problems with a strong interfacial contact discontinuity, and highlight the superior performance of the positivity-preserving Lagrangian method for such problems. In this problem, the fluid at the left side of the membrane with the position of $x = 0.3$ is a perfect gas. The fluid at the right side of the membrane is water and is modeled as a stiffened gas. The initial states of two fluids and the constants of their EOS are as follows,

$$\begin{cases} (\rho, u, p, \gamma) = (5, 0, 10^5, 1.4), & 0 \le x \le 0.3 \\ (\rho, u, p, \gamma, p_c) = (1000, 0, 10^9, 4.4, 6 \times 10^8), & 0.3 < x \le 1.0. \end{cases}$$

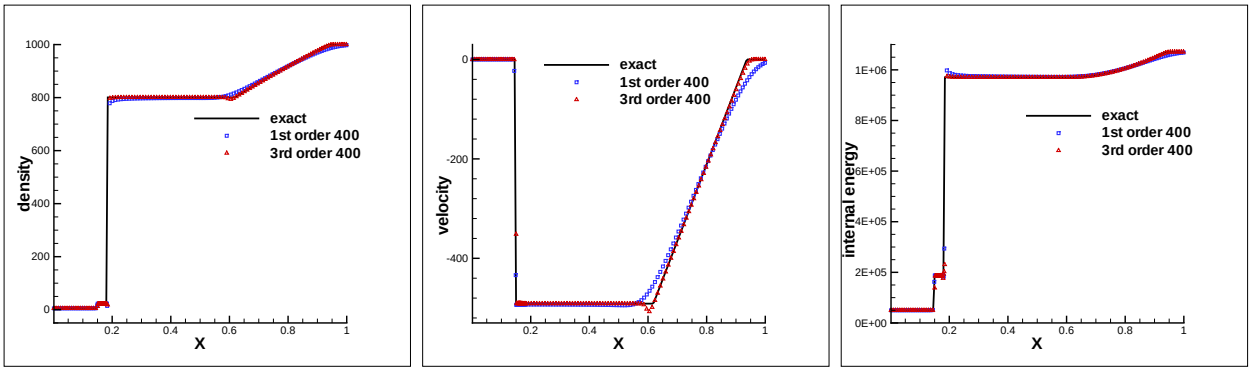

Figure 4.5: The results of the water-air shock tube problem with 200 cells at $t = 0.00024$. Left: density; Middle: velocity; Right: internal energy.

The results of density, velocity and internal energy at $t = 0.00024$ by the first and third order positivity-preserving Lagrangian schemes with 200 initially uniform cells are shown in Figure 4.5. The agreement between the exact and numerical solutions is very good, despite of the very tough initial conditions. The front of the interface is captured very sharply which shows the advantage of the Lagrangian method. The results also demonstrate that the schemes can preserve the positivity of density and internal energy well and the high order scheme can produce results with better resolution.

Example 4.6. *The spherical underwater explosion of a TNT charge.*

This 1D spherically symmetric underwater detonation problem is often applied as a benchmark to test the robustness of numerical methods for multi-phase problems with strong shocks and contact discontinuities.

The charge is a 3-cm-radius TNT sphere. The initial condition consists of the detonation-products phase (left) and the water phase (right). In this paper, in order to test the performance of our schemes on the property of positivity-preserving in the simulation of this kind of multi-material problems with complicated EOS, we take the original model given in the references such as in [11], and scale the values of the variables related to density and pressure such as ρ, p and the constants A_1, A_2 which appear in the JWL EOS by 10^{-6}, to increase the stiffness of the problem and to make the appearance of negative density and

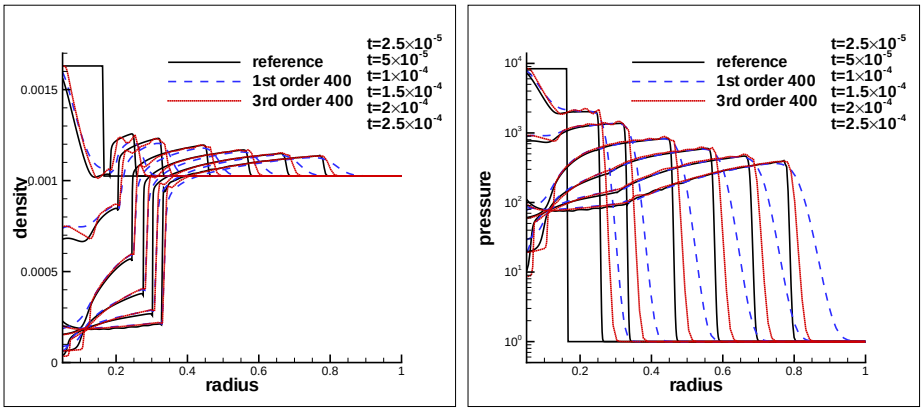

Figure 4.6: The results of the spherical underwater explosion of a TNT charge with 400 cells at several typical times. Left: density; Right: pressure.

internal energy more likely. Thus the initial condition is as follows,

$$\begin{cases} (\rho, u, p) = (1.63 \times 10^{-3},\ 0,\ 8.381 \times 10^{3}), & 0 \le x \le 0.16 \\ (\rho, u, p) = (1.025 \times 10^{-3},\ 0,\ 1.), & 0.16 < x \le 3. \end{cases}$$

The gaseous product of the detonated explosive is modeled by the JWL EOS (2.7) with $A_1 = 3.712 \times 10^5$, $A_2 = 3.23 \times 10^3$, $\rho_0 = 1.63 \times 10^{-3}$, $R_1 = 4.15$, $R_2 = 0.95$ and $\gamma = 1.3$. The water is modeled by the stiffened EOS (2.6) with $\gamma = 7.15$ and $p_c = 3.309 \times 10^2$.

Figure 4.6 plots the results of the first and third order positivity-preserving Lagrangian schemes in spherical coordinates with 400 initially uniform cells at several typical time. The reference solution is obtained by the first order Lagrangian scheme in the one-dimensional spherical coordinate with 2000 grid cells. The Lagrangian scheme shows the advantage in capturing the interface of the gas and condensed phases of an underwater explosion automatically and sharply. Both density and pressure can always keep positivity in this problem. The higher order scheme produces better resolution for both density and pressure. The shape of density and pressure at different time is also comparable to those shown in [11].

4.2 Two-dimensional tests

Example 4.7. *Numerical convergence study.*

We test the numerical convergence of our first and second order positivity-preserving Lagrangian schemes in this example. In the Cartesian coordinates, we choose the standard

Table 4.3: Errors of the first order Lagrangian scheme for the vortex problem using $N_x \times N_y$ initially uniform mesh cells.

$N_x = N_y$	Norm	Density	order	Momentum	order	Energy	order
20	L_1	0.30E-2		0.10E-1		0.15E-1	
	L_∞	0.45E-1		0.99E-1		0.29E+0	
40	L_1	0.13E-2	1.25	0.43E-2	1.23	0.68E-2	1.14
	L_∞	0.20E-1	1.15	0.46E-1	1.12	0.13E+0	1.12
80	L_1	0.57E-3	1.16	0.20E-2	1.15	0.31E-2	1.13
	L_∞	0.90E-2	1.16	0.22E-1	1.03	0.61E-1	1.12
160	L_1	0.27E-3	1.09	0.92E-3	1.08	0.15E-2	1.07
	L_∞	0.42E-2	1.11	0.10E-1	1.10	0.29E-1	1.07

two-dimensional vortex evolution problem (e.g. [32]) as our accuracy test function. The vortex problem is described as follows: the mean flow is $\rho = 1$, $p = 1$ and $(u, v) = (1, 1)$. We add to this mean flow an isentropic vortex perturbations in (u, v) and the temperature $T = p/\rho$, no perturbation in the entropy $S = p/\rho^\gamma$.

$$(\delta u, \delta v) = \frac{\epsilon}{2\pi} e^{0.5(1-r^2)}(-\overline{y}, \overline{x}), \qquad \delta T = -\frac{(\gamma-1)\epsilon^2}{8\gamma\pi^2} e^{(1-r^2)}, \qquad \delta S = 0$$

where $(-\overline{y}, \overline{x}) = (x-5, y-5)$, $r^2 = \overline{x}^2 + \overline{y}^2$, and the vortex strength is $\epsilon = 10.0828$ such that the lowest density and lowest pressure of the exact solution are 7.8×10^{-15} and 1.7×10^{-20} respectively.

The computational domain is taken as $[0, 10] \times [0, 10]$, and periodic boundary conditions are used. For this problem, the second order Lagrangian scheme without the positivity-preserving limiter fails to calculate due to the appearance of the negative internal energy. The convergence results for the first order Lagrangian scheme and the second order ENO Lagrangian scheme with the positivity-preserving limiter at $t = 0.1$ are listed in Tables 4.3-4.4. The percentage of the cells that need the usage of the positivity-preserving limiter is listed in Table 4.4 as well. In the tables, we can see the expected first and second order accuracy for all the conserved variables such as density, momentum and total energy, especially in the L_1 norm.

Example 4.8. *The Sedov blast wave problem in a Cartesian coordinate system [25]*

Table 4.4: Errors of the second order ENO Lagrangian scheme with the positivity-preserving limiter for the vortex problem using $N_x \times N_y$ initially uniform mesh cells.

$N_x = N_y$	Norm	Density	order	Momentum	order	Energy	order	limited cells
20	L_1	0.26E-2		0.73E-2		0.13E-1		1%
	L_∞	0.37E-1		0.93E-1		0.26E+0		
40	L_1	0.73E-3	1.85	0.20E-2	1.90	0.36E-2	1.84	0.32%
	L_∞	0.12E-1	1.67	0.27E-1	1.80	0.70E-1	1.90	
80	L_1	0.19E-3	1.94	0.50E-3	1.96	0.90E-3	1.98	0.11%
	L_∞	0.36E-2	1.68	0.84E-2	1.66	0.22E-1	1.69	
160	L_1	0.48E-4	1.98	0.13E-3	1.98	0.23E-3	1.98	0.029%
	L_∞	0.12E-2	1.60	0.25E-2	1.75	0.68E-2	1.68	

The Sedov blast wave problem models the expanding wave by an intense explosion in a perfect gas. The simulation is performed on a Cartesian grid whose initial uniform grid consists of 60×60 rectangular cells with a total edge length of 1.2 in both directions. The initial density is unity and the initial velocity is zero. The specific internal energy is zero except in the first zone where it has a value of 182.09. But in the practical simulation, as we cannot simulate vacuum, we usually set up p to be a small positive value such as 10^{-6}. Here we take p to be a smaller positive value, that is 10^{-14} which is demonstrated to bring much more challenge to the scheme. In fact, the second order Lagrangian scheme without the positivity-preserving limiter fails to calculate. Reflective boundary conditions are used on the four boundaries. The analytical solution gives a shock at radius unity at time unity with a peak density of 6. Figure 4.7 shows the results by the purely Lagrangian calculations at the time $t = 1$. We can clearly see that the positivity of density and pressure can be kept well for our schemes and the higher order ENO scheme obtains more symmetrical and precise solution than the first order scheme.

Example 4.9. *The Saltzman problem [8]*

The problem consists of a rectangular box whose left end is a piston. The piston moves into the box with a constant velocity of 1.0. The initial grid is designed to be not aligned with the fluid flow to validate the robustness of a Lagrangian scheme. The initial grid is 100

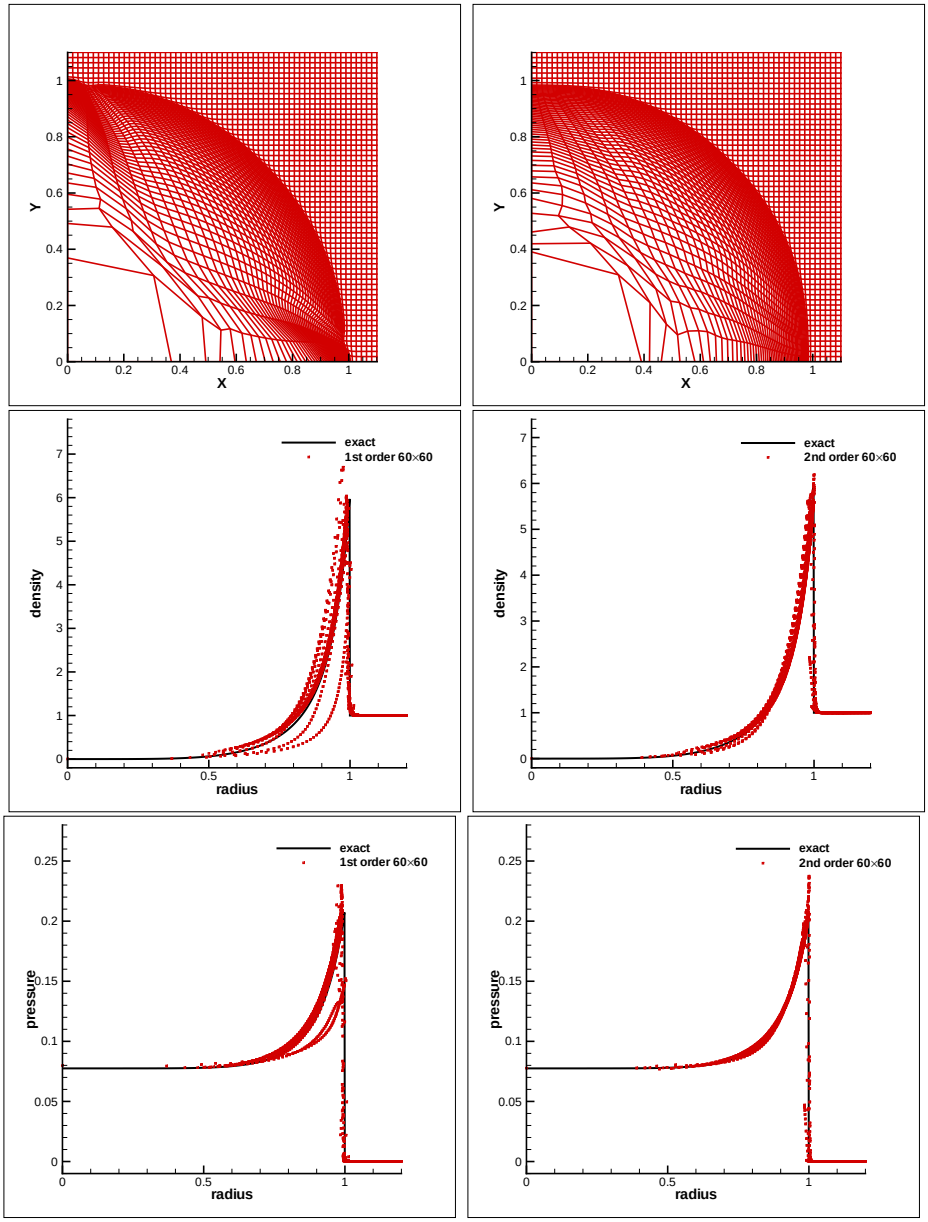

Figure 4.7: The results of the first and second order positivity-preserving Lagrangian schemes for the Sedov problem. Top row: grid. Middle row: density versus radius. Bottom row: pressure versus radius. Left: first order; Right: second order.

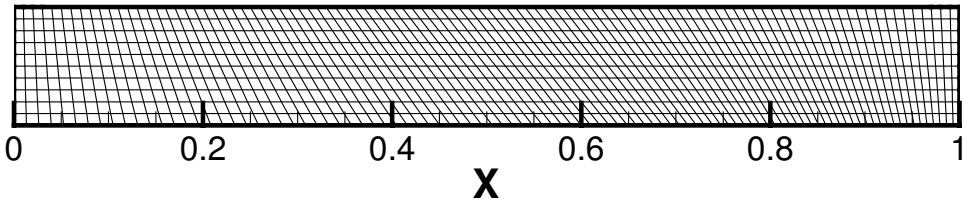

Figure 4.8: The initial grid of the Saltzman problem.

cells in the x-direction and 10 cells in the y-direction which is defined by

$$x(i,j) = (i-1)\Delta x + (11-j)\sin(0.01\pi(i-1))\Delta y, \qquad y(i,j) = (j-1)\Delta y$$

where $\Delta x = \Delta y = 0.01$. The initial grid is displayed in Figure 4.8. The working fluid is described by a perfect gas with $\gamma = 5/3$. The initial condition is $\rho = 1$, $u = 0$, $v = 0$ and $p = 0$. Similarly as in the above example, in practical simulation we take p to be a much smaller positive value, that is 10^{-14} to demonstrate the robustness of the scheme. For this problem, the second order Lagrangian scheme without the positivity-preserving limiter will blow up due to the appearance of negative pressure. Reflective boundary conditions are used on the right, upper and lower boundaries. The numerical results for the first order Lagrangian scheme and the second order Lagrangian scheme with the positivity-preserving limiter are shown in Figures 4.9 at the time $t = 0.6$. The analytic post shock density is 4.0 and the shock speed is 1.333. At this time, the shock is expected to be located at $x = 0.8$. We can observe that our first and second order schemes can keep the positivity of density and pressure well and the higher order scheme preserves the one-dimensional solution well except for the region near the top and bottom wall boundaries where the results are affected by the boundary conditions. Also the higher order scheme gives better shock resolution for this example.

Example 4.10. *The air-water-air problem [26]*

In this test, we consider a radially symmetric two-phase problem. A 1.2-radius cylinder

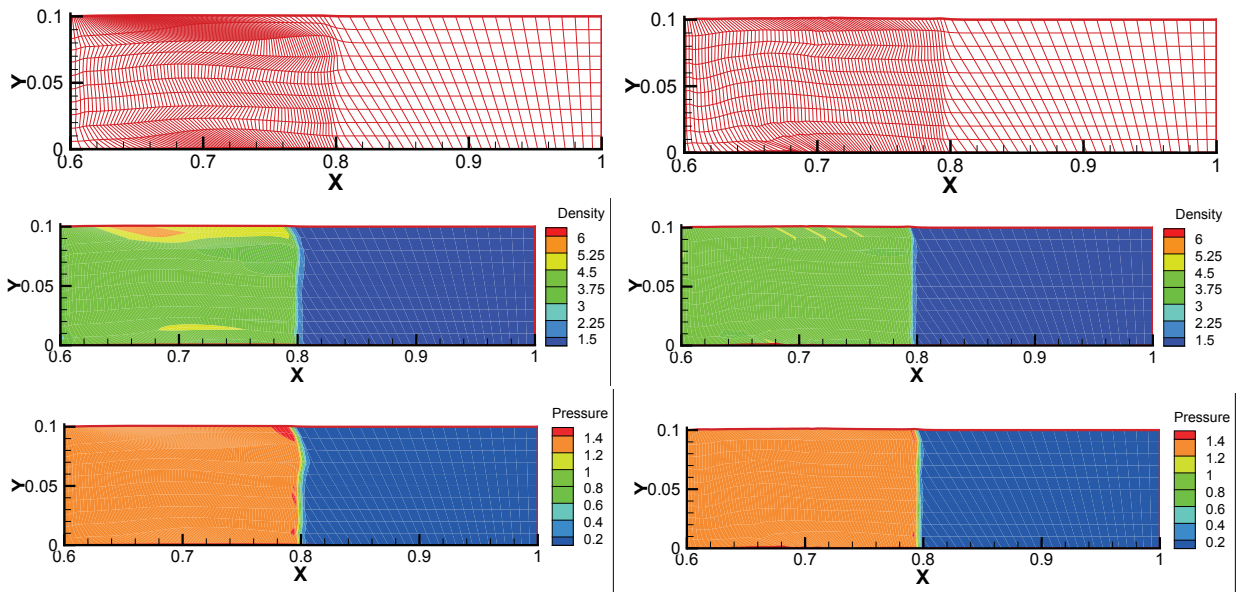

Figure 4.9: The results of the first and second order positivity-preserving Lagrangian schemes for the Saltzman problem at $t = 0.6$. Top row: grid; Middle row: density contour; Bottom row: pressure contour. Left: first order; Right: second order.

consists of air ($r \in [0, 0.2]$), water ($r \in [0.2, 1.0]$) and air ($r \in [1.0, 1.2]$). Its specific initial condition is as follows,

$$(\rho, u, v, p, \gamma, p_c) = \begin{cases} (1000, 0, 0, 0.001, 1.4, 0), & 0 \le r \le 0.2 \\ (1, 0, 0, 1, 7, 3000), & 0.2 < r \le 1.0 \\ (0.001, 0, 0, 0.001, 1.4, 0), & 1.0 < r \le 1.2. \end{cases} \tag{4.1}$$

Because of the symmetry of the solution, we only simulate a quarter of the domain, and apply the symmetric boundary conditions to the bottom, left and right sides during the computations.

Figure 4.10 shows the results of grid, density, velocity and internal energy for our second order positivity-preserving Lagrangian scheme with 100×10 initially equal-angle cells at the typical time $t = 0.0015, 0.003, 0.007$. This problem cannot be solved by the second order Lagrangian scheme without the positivity-preserving limiter due to the negativity of the internal energy. From the figures, we observe that the positivity of density and internal energy can be kept well during the whole process. Figure 4.11 shows the contour results of density, velocity and internal energy cuts along each radial grid line for the first and second order positivity preserving Lagrangian schemes. The reference exact solution is obtained by

the one-dimensional first order Lagrangian scheme in the cylindrical coordinate with 2000 cells. By the comparison, the second order scheme is shown to have a better resolution.

5 Concluding remarks

In this paper, we discuss the methodology to construct positivity-preserving Lagrangian schemes in one- and two-dimensional spaces for compressible Euler equations with general equations of state. Firstly we develop a positivity-preserving approximate HLLC Riemann solver for the Lagrangian scheme and present a class of first order positivity-preserving Lagrangian schemes. Then we design a class of high order positivity-preserving Lagrangian schemes both in one- and two-dimensional spaces by using the essentially non-oscillatory (ENO) reconstruction, the strong stability preserving (SSP) high order time discretizations and the positivity-preserving limiter which can be proven to maintain conservation and uniformly high order accuracy. The numerical results of multi-material problems with the general EOS demonstrate the effectiveness of our first order and high order positivity-preserving Lagrangian schemes. The schemes can also be extended to the higher (than second) order schemes if curvilinear grids are applied in the two-dimensional space [7, 18]. The generalization of the positivity-preserving Lagrangian schemes to cylindrical coordinates and further improvement of the scheme robustness (for example with respect to mesh movement quality, geometric conservation law, and symmetry-preserving) constitute our future work.

References

[1] P. Batten, N. Clarke, C. Lambert and D. Causon, *On the choice of wavespeeds for the HLLC Riemann solver*, SIAM Journal on Scientific Computing, 18 (1997), 1553-1570.

[2] F. Bezard and B. Despres, *An entropic solver for ideal Lagrangian magnetohydrodynamics*, Journal of Computational Physics, 154 (1999), 65-89.

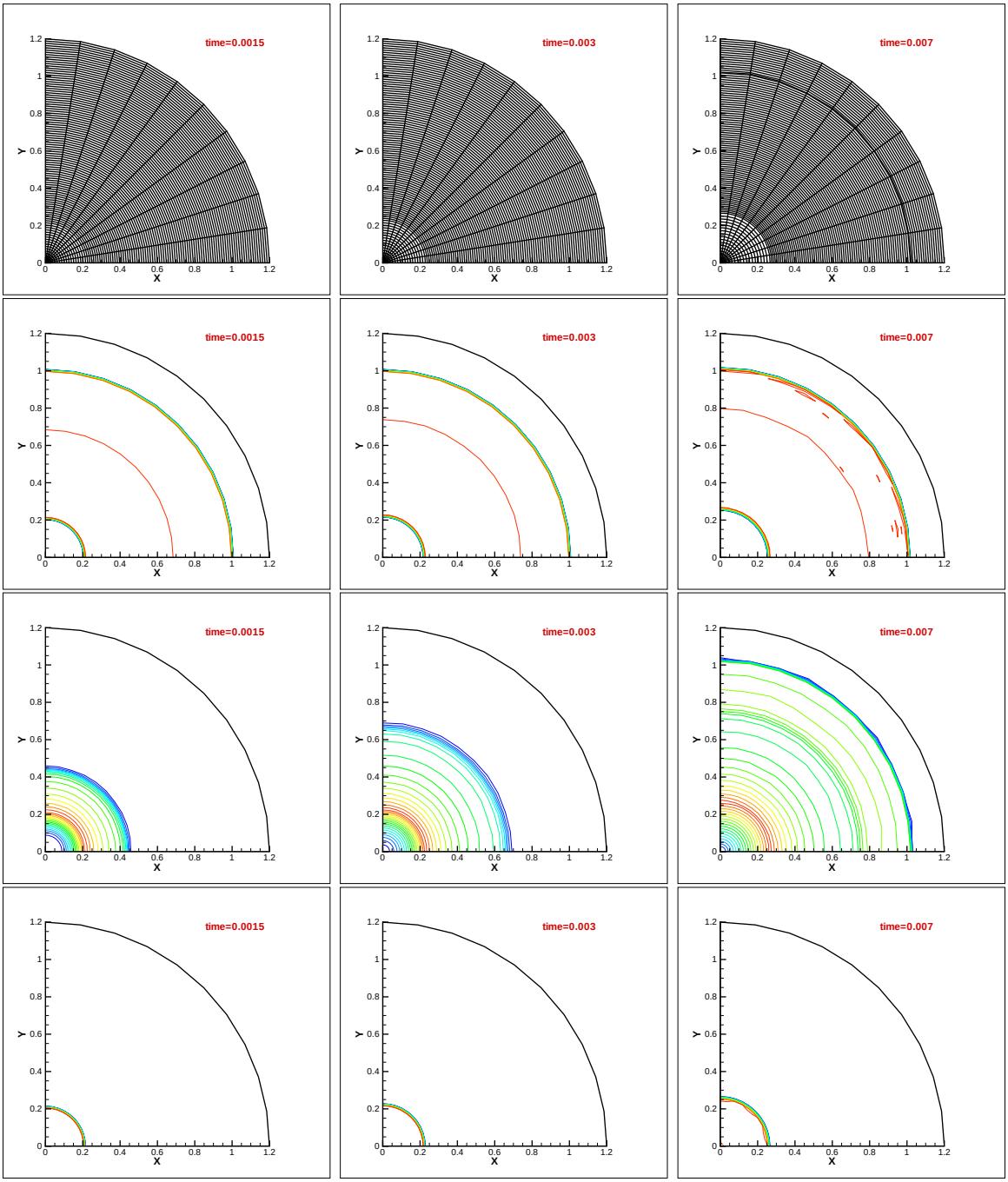

Figure 4.10: The results of the second order positivity-preserving Lagrangian scheme for the air-water-air problem. Top row: grid; Second row: density; Third row: velocity; Bottom row: internal energy. Left: $t = 0.0015$; Middle: $t = 0.003$; Right: $t = 0.007$.

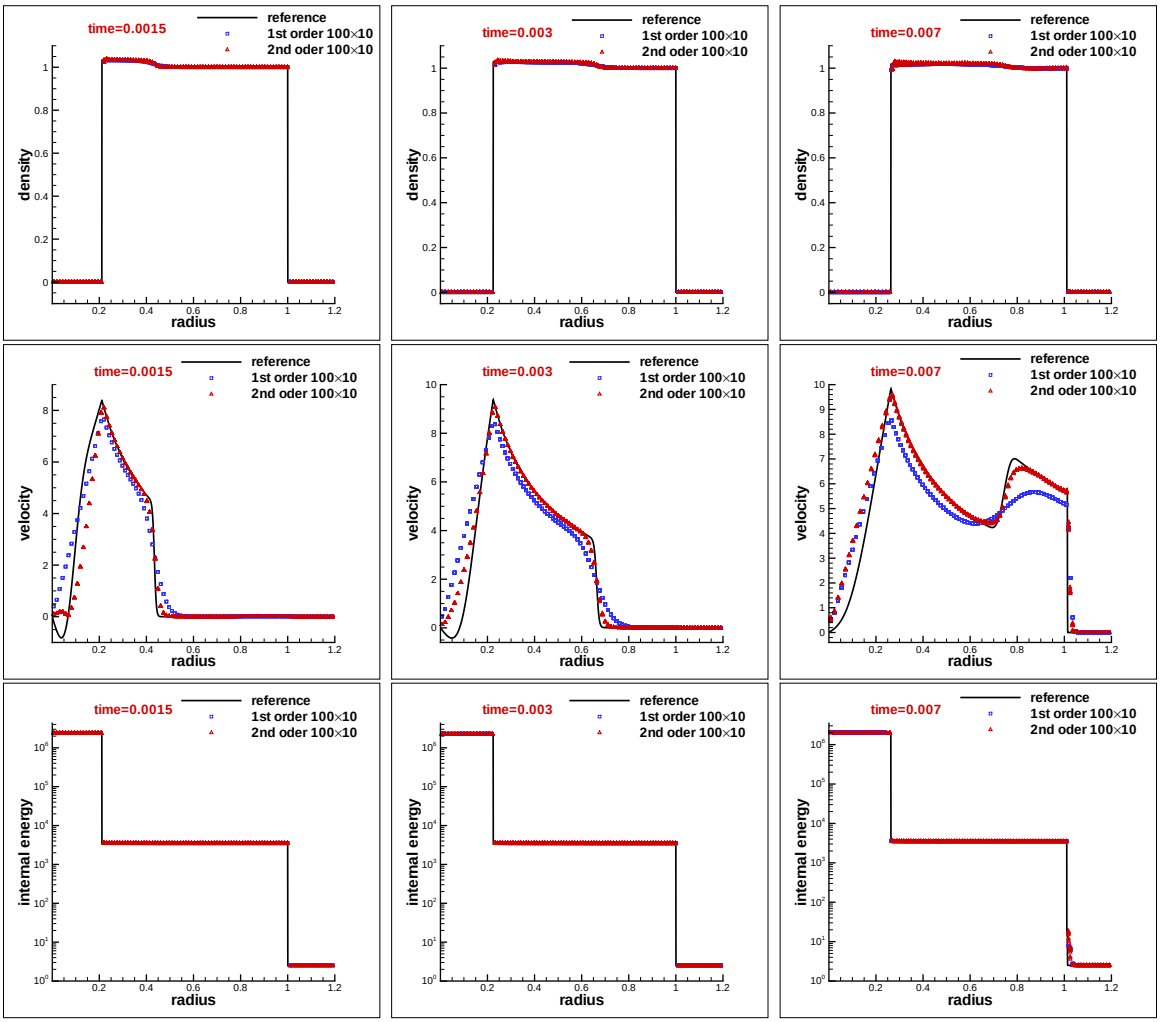

Figure 4.11: The cut contour results of the first and second order positivity-preserving Lagrangian schemes for the air-water-air problem compared with the reference solution. Top row: density; Middle row: velocity; Bottom row: internal energy. Left: $t = 0.0015$; Middle: $t = 0.003$; Right: $t = 0.007$.

[3] E.J. Caramana, D.E. Burton, M.J. Shashkov and P.P. Whalen, *The construction of compatible hydrodynamics algorithms utilizing conservation of total energy*, Journal of Computational Physics, 146 (1998), 227-262.

[4] G. Carré, S. Del Pino, B. Després and E. Labourasse, *A cell-centered Lagrangian hydrodynamics scheme in arbitrary dimension*, Journal of Computational Physics, 228 (2009), 5160-5183.

[5] J. Cheng and C.-W. Shu, *A high order ENO conservative Lagrangian type scheme for the compressible Euler equations*, Journal of Computational Physics, 227 (2007), 1567-1596.

[6] J. Cheng and C.-W. Shu, *A high order accurate conservative remapping method on staggered meshes*, Applied Numerical Mathematics, 58 (2008), 1042-1060.

[7] J. Cheng and C.-W. Shu, *A third order conservative Lagrangian type scheme on curvilinear meshes for the compressible Euler equation*, Communications in Computational Physics, 4 (2008), 1008-1024.

[8] J.K. Dukowicz and B.J.A. Meltz, *Vorticity errors in multidimensional Lagrangian codes*, Journal of Computational Physics, 99 (1992), 115-134.

[9] B. Einfeldt, C.D. Munz, P.L. Roe and B. Sjögreen, *On Godunov-type methods near low densities*, Journal of Computational Physics, 92 (1991), 273-295.

[10] J.L. Estivalezes and P. Villedieu, *High-order positivity preserving kinetic schemes for the compressible Euler equations*, SIAM Journal on Numerical Analysis, 33 (1996), 2050-2067.

[11] C. Farhat, J.-F. Gerbeau and A. Rallu, *FIVER: A finite volume method based on exact two-phase Riemann problems and sparse grids for multi-material flows with large density jumps*, Journal of Computational Physics, 231 (2012), 6360-6379.

[12] G. Gallice, *Positive and entropy stable Godunov-type schemes for gas dynamics and MHD equations in Lagrangian or Eulerian coordinates*, Numerische Mathematik, 94 (2003), 673-713.

[13] J. Gressier, P. Villedieu and J.-M. Moschetta, *Positivity of flux vector splitting schemes*, Journal of Computational Physics, 155 (1999), 199-220.

[14] A. Harten, P.D. Lax and B. Van Leer, *On upstream differencing and Godunov-type schemes for hyperbolic conservation laws*, SIAM Review, 25 (1983), 35-61.

[15] G.-S. Jiang and C.-W. Shu, *Efficient implementation of weighted ENO schemes*, Journal of Computational Physics, 126 (1996), 202-228.

[16] T. Linde and P.L. Roe, *Robust Euler codes*, Thirteenth Computational Fluid Dynamics Conference, AIAA Paper 97-2098.

[17] M. Liou, *A sequel to AUSM: AUSM+*, Journal of Computational Physics, 129 (1996), 364-382.

[18] W. Liu, J. Cheng and C.-W. Shu, *High order conservative Lagrangian schemes with Lax-Wendroff type time discretization for the compressible Euler equations*, Journal of Computational Physics, 228 (2009), 8872-8891.

[19] P.-H. Maire, *A high-order cell-centered Lagrangian scheme for two-dimensional compressible fluid flows on unstructured meshes*, Journal of Computational Physics, 228 (2009), 2391-2425.

[20] C.D. Munz, *On Godunov-type schemes for Lagrangian gas dynamics*, SIAM Journal on Numerical Analysis, 31 (1994), 17-42.

[21] B. Perthame, *Boltzmann type schemes for gas dynamics and the entropy property*, SIAM Journal on Numerical Analysis, 27 (1990), 1405-1421.

[22] B. Perthame, *Second-order Boltzmann schemes for compressible Euler equations in one and two space dimensions*, SIAM Journal on Numerical Analysis, 29 (1992), 1-19.

[23] B. Perthame and C.-W. Shu, *On positivity preserving finite volume schemes for Euler equations*, Numerische Mathematik, 73 (1996), 119-130.

[24] R. Saurel and R. Abgrall, *A simple method for compressible multifluid flows*, SIAM Journal on Scientific Computing, 21 (1999), 1115-1145.

[25] L.I. Sedov, *Similarity and Dimensional Methods in Mechanics*, Academic Press, New York, 1959.

[26] K.-M. Shyue, *A fluid-mixture type algorithm for barotropic two-fluid flow problems*, Journal of Computational Physics, 200 (2004), 718-748.

[27] T. Tang and K. Xu, *Gas-kinetic schemes for the compressible Euler equations I: positivity-preserving analysis*, Zeitschrift für angewandte Mathematik und Physik ZAMP, 50 (1999), 258-281.

[28] E.F. Toro, *Riemann Solvers and Numerical Methods for Fluid Dynamics*, Springer-Verlag, Berlin, 1999.

[29] X. Zhang and C.-W. Shu, *On positivity preserving high order discontinuous Galerkin schemes for compressible Euler equations on rectangular meshes*, Journal of Computational Physics, 229 (2010), 8918-8934.

[30] X. Zhang and C.-W. Shu, *Positivity preserving high order discontinuous Galerkin schemes for compressible Euler equations with source terms*, Journal of Computational Physics, 230 (2011), 1238-1248.

[31] X. Zhang and C.-W. Shu, *Maximum-principle-satisfying and positivity preserving high order schemes for conservation laws: Survey and new developments*, Proceedings of the Royal Society A, 467 (2011), 2752-2776.

[32] X. Zhang and C.-W. Shu, *positivity preserving high order finite difference WENO schemes for compressible Euler equations*, Journal of Computational Physics, 231 (2012), 2245-2258.